Received: 19 November 2024 | Revised: 10 July 2025 | Accepted: 12 July 2025

DOI: 10.1002/mp.18040

RESEARCH ARTICLE

MEDICAL PHYSICS

Development and validation of a Monte Carlo model of a mobile accelerator for intraoperative radiation therapy

Rafael Ayala[1,2] | **Álvaro Soza**[1] | **María Jesús García**[1] | **Rocío García**[1] | **José Manuel Udías**[2,3] | **Paula Ibáñez**[2,3]

[1]Servicio de Dosimetría y Radioprotección, Hospital General Universitario Gregorio Marañón, Madrid, Spain

[2]Nuclear Physics Group and IPARCOS, Department of Structure of Matter, Thermal Physics and Electronics, CEI Moncloa, Universidad Complutense de Madrid, Madrid, Spain

[3]Instituto de Investigación Sanitaria del Hospital Clínico San Carlos, Madrid, Spain

Correspondence
Rafael Ayala, Servicio de Dosimetría y Radioprotección, Hospital General Universitario Gregorio Marañón, Dr. Esquerdo 46, 28007, Madrid, Spain.
Email: rafayala@ucm.es

Funding information
Spanish Government and Next Generation EU Recovery and Resilience Facility, Grant/Award Numbers: INVENTOR-PID2022-137114OA-I00, FLASHonCHIP-PLEC2022-009256, PROTOTWIN-TED2021-130592B-I00; Comunidad de Madrid (Community of Madrid), Grant/Award Number: ASAP-CM-S2022/BMD7434; European Union - RETIMAGER, Grant/Award Number: 101099096

Abstract

Background: Intraoperative electron radiation therapy (IOERT) relies on accurate and precise dose delivery to the tumor or tumor bed using mobile accelerators and interchangeable applicators, while critical organs are typically displaced or shielded during surgery. Treatment planning and linac commissioning are often based on water measurements, Monte Carlo (MC) simulations of the accelerator head and applicator system provide detailed insights into dose distributions and beam characteristics, offering additional support for clinical evaluation.

Purpose: This study develops an MC model of the Liac HWL mobile accelerator using a hypothetical linac head geometry, due to the limited availability of detailed information on its internal components resulting from manufacturer disclosure policies. The model is optimized by adjusting three geometric parameters of the linac head and the initial beam energy spectrum to match experimental data. Additionally, it provides a set of Phase Space Files (PSFs) to support research and clinical applications.

Methods: The MC code PENELOPE, integrated with the penEasy framework, was used to simulate the Liac HWL. The hypothetical head geometry was defined by parameters such as the inner diameter of the head, the thickness of the scattering foil, and the thickness of the exit window. Output factors (OFs), percentage depth doses (PDDs), and off-axis ratios (OARs) were calculated in a virtual water phantom for different applicator sizes, bevel angles, and energies. Gamma analysis was employed to validate the model by comparing calculated and measured dose distributions. PSFs were made available in the IAEA PHSP format at four energies (6, 8, 10, and 12 MeV).

Results: The model matched measured OFs within 2.5%. PDDs and OARs met the gamma analysis criteria (2% dose difference and 1 mm distance-to-agreement) in more than 93% of the studied cases, with the worst-case scenario occurring for the smallest applicator (3 cm diameter) with a 45° bevel angle at 6 MeV, resulting in OAR gamma passing rates of 85.7% at z_{max} and 86.1% at R_{90}.

Conclusions: Despite the use of a hypothetical geometry, the model offers accurate dosimetric data and practical guidance for IOERT commissioning and treatment planning. It highlights potential dosimetric issues, particularly the lack of homogeneity in OARs for large-diameter applicators, and allows fine-tuning based on real-world data. Additionally, the PSFs generated in this study

provide a reliable resource for simulating IORT dose distributions and analyzing the characteristics of IOERT beams.

KEYWORDS
IORT, IOERT, Liac HWL, Monte Carlo

1 | INTRODUCTION

Intraoperative radiation therapy (IORT) is a technique used to deliver a single high dose of radiation directly to the tumor or tumor bed during surgery. The goal of IORT is to maximize the dose to the target area while minimizing the absorbed dose to nearby healthy tissues, which is often achieved by physically displacing or shielding them with protective materials.[1,2] However, the removal of tissues and repositioning of anatomical structures during surgery alters the patient's geometry, making it challenging to base dosimetry calculations on pre-operative imaging.

Intraoperative electron radiation therapy (IOERT), a specific form of IORT, uses electron beams delivered through interchangeable applicators of various sizes to conform the absorbed dose to the tumor or tumor bed. The state-of-the-art in IOERT involves the use of mobile accelerators that can be brought directly into the operating room. These mobile units deliver high dose rates ranging from 10 to 40 Gy per minute, with doses per pulse of up to several cGy, enabling shorter treatment times ($\approx$ 100 s) and improved flexibility in the surgical setting compared to IOERT performed with conventional linacs.[3]

During the IOERT procedure, the radiation oncologist determines the applicator size, its orientation, bevel angle, and the desired electron therapeutic range based on their medical judgment and the real-time information obtained during surgery. The absorbed dose to the target is typically prescribed beforehand as part of the overall treatment strategy, although in some cases it may be adjusted intraoperatively depending on surgical findings. Based on these inputs, the medical physicist calculates the treatment plan, selecting the appropriate beam energy and determining the necessary monitor units. The goal is to ensure that the 90% isodose covers the tumor or tumor bed with an adequate margin, typically encompassing areas of residual disease or high-risk tissue.[1,4–8] The reliance on intraoperative decision-making, rather than pre-operative planning, complicates the process of planning radiation therapy in advance.[9]

In response to this issue, a treatment planning system similar to those used in external beam radiotherapy was developed.[10] This system enables absorbed dose calculations based on CT images of the patient, enhancing the accuracy of dosimetry during IOERT.

However, despite this development, a fundamental challenge in IORT remains unresolved in most clinics: intraoperative imaging has yet to become standard practice. As a result, treatment planning is typically performed using hand calculations of monitor units based on measurements in water phantoms, rather than patient-specific anatomical data. Monitor units are determined from output factors (OFs), and energy selection relies on percentage depth dose (PDD) profiles. The expected shape of the isodose curves is inferred from off-axis ratios (OAR) and PDD profiles, but this approach provides only an oversimplified representation of the absorbed dose distribution in the actual patient. The magnitude of this limitation depends on tissue heterogeneity; for soft tissue cases, deviations in absorbed dose are expected to be within approximately 5%, while more complex anatomical scenarios–such as unshielded breast treatments–may result in more substantial dose inaccuracies in structures like ribs or lung.

Depending on the required level of accuracy, different approaches can be used for absorbed dose calculation in IOERT. Water-based measurements remain a widely accepted standard in most clinical scenarios and are typically sufficient for routine treatments. However, in anatomically complex situations or when dose gradients are steep, higher accuracy may be beneficial. In such cases, a well-defined model of the linear accelerator enables a more precise and accurate prediction of dose distributions, helping optimize treatment parameters. Monte Carlo (MC) models, in particular, excel in this task due to their ability to simulate particle interactions with high accuracy, offering detailed insights into the behavior of the beam under various conditions.[11]

MC simulations have been widely employed to characterize and validate the dosimetric properties of mobile linacs used for IOERT, such as the Liac, Novac7,[12–16] and Mobetron 1000.[17] These studies have demonstrated the high accuracy of MC methods in reproducing experimentally determined dose distributions, providing valuable information about beam characteristics. However, a substantial challenge remains due to the limited disclosure by manufacturers regarding the geometries and materials of the inner components of accelerator heads. This issue is particularly relevant to the Liac HWL model, for which detailed technical information is currently scarce. Although the manufacturer provides software displaying MC-calculated isodoses in water, no

details of these simulations are disclosed, and several applicators are not included.

The issue of limited information about linac head geometries is a well-known problem. Previous works[18,19] have demonstrated the feasibility of producing an IORT MC model by reconstructing phase space files (PSFs) directly from experimental measurements.

In this paper, however, we have opted for a different approach. We describe the development of an MC model for the Liac HWL mobile accelerator, constructed using available information and a simplified hypothetical geometry. This work builds on a previous accelerator design from the same company, where material properties and internal geometries were well-documented.[12] We will validate this model extensively and present a representative set of dose distributions to provide a comprehensive understanding of the dosimetric characteristics of the linac.

With these calculated dose distributions, we will be able to evaluate whether the linac delivers dose distributions that conform to the expected dosimetric characteristics of IOERT beams, which may not be readily apparent from typical measurements. Visualizing MC dose distributions in water facilitates the analysis of various applicator and energy combinations, enabling an assessment of their clinical acceptability and helping determine if any adjustments are required to achieve the desired dose to the target.

Although this study focuses on a specific accelerator model, it aims to provide a methodology that can aid in the modeling of other intraoperative linacs, serving as a reference for their MC simulation. Additionally, the simulation of this particular linac can support further research on various aspects of IOERT, including detector development, shielding assessment, and applicator design.

2 | MATERIAL AND METHODS

2.1 | Liac HWL

The linear accelerator under study is the Liac HWL model from Sordina IORT Technologies (S.I.T.), which provides electron energies of 6, 8, 10, and 12 MeV. The available applicators are cylindrical in shape, made of polymethyl methacrylate (PMMA) with a wall thickness of 0.5 cm and a hard-docking design. The inner diameters range from 3 to 10 cm in 1 cm increments, along with an additional applicator with a nominal diameter of 12 cm, which, at least in the set provided with the unit under study, actually measures 12.3 cm. Each applicator of a specific diameter can also terminate with one of four different bevel angles: 0, 15, 30 and 45 degrees. For clarity throughout this work, an applicator of diameter d and bevel ending α will be denoted as C_dB_α.

TABLE 1 Beam characteristics of the reference applicator $C_{10}B_0$, where PRF stands for pulse repetition frequency, and z_{max} and R_{50} denote the depth of maximum dose and the depth at 50% dose, respectively.

	Beam characteristics $C_{10}B_0$			
Energy (MeV)	**6**	**8**	**10**	**12**
PRF (Hz)	25	20	15	10
Dose per pulse (cGy/p)	1.01	1.77	3.04	4.37
z_{max} (cm)	0.8	1.1	1.2	1.4
R_{50} (cm)	2.3	2.9	3.7	4.4

The applicators have an overall length of 40 cm, consisting of two sections: one that is common to all applicators of the same diameter and another that differs in its beveled ending, which can have the angles listed above. The manufacturer offers two different applicator sets with varying section lengths. Set 1, as referenced in Winkler et al.,[20] includes sections measuring 16.5 and 23.5 cm, while Set 2 comprises sections of 10.5 and 29.5 cm. All measurements in this study were performed with applicators from Set 2, as this was the set provided to us.

We have considered the applicators to be positioned, such that their distal end is located at $z = 0$ cm, with the linac aligned along the z-axis. Each applicator has a total length of 40 cm. The first 36.8 cm maintain a constant inner diameter, corresponding to the nominal applicator diameter. This section is followed by a conical transition that adjusts the inner diameter to 7 cm. The final segment is a 2 cm-long cylindrical section with a 7 cm diameter, connecting to the accelerator head at $z = 40$ cm. Beyond this point, the aperture narrows through a conical section, reaching a 4 cm diameter at the exit window ($z = 49.2$ cm). For z>49.2 cm, which corresponds to the linac head, the only disclosed manufacturer detail is the source-to-surface distance (SSD) of 64.5 cm, where the lower plane of the scattering foil is positioned (Figure 1).

For beveled applicators, the total length is measured along the beam axis (geometrical axis), ensuring that the SSD remains consistent along this direction; thus, the total length along the beam axis remains 40 cm, regardless of bevel angle.

Regarding the linac's dosimetric properties, the dose per pulse reaches a maximum of approximately 7 cGy/p with the C_4B_{45} applicator at 12 MeV. For flat applicators only, a maximum dose of 6.5 cGy/p is observed with the C_4B_0 at 12 MeV. Additional beam characteristics for the reference applicator, obtained during the acceptance tests of the machine, are provided in Table 1.

2.2 | Measurements

The machine was characterized with measurements in water in an IBA Blue Phantom^2 3D beam analyzer. PDDs

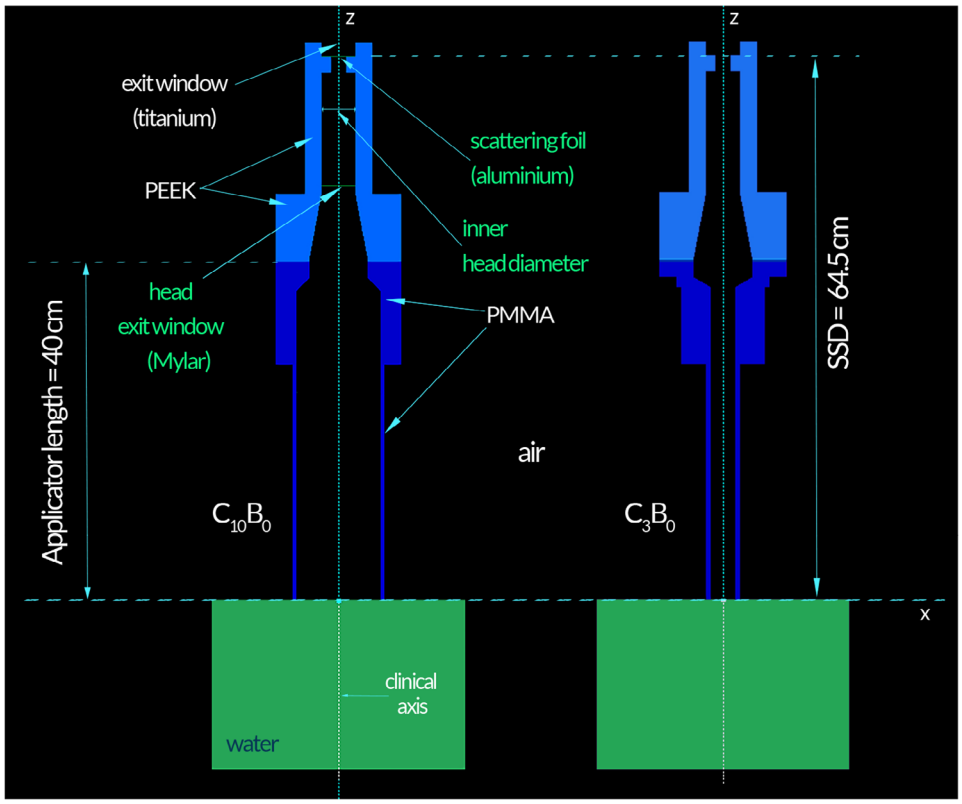

FIGURE 1 2D view of the simulated geometry of the Liac HWL with the $C_{10}B_0$ and C_3B_0 applicators. Labels for the three elements adjusted during model optimization–the inner cylindrical head (diameter), the scattering foil (thickness), and the Mylar exit window (thickness)–are highlighted in green. The SSD, applicator length, and materials used in the simulation are also labeled in the figure. SSD, source-to-surface distance.

and OFs for all possible combinations of applicator diameter, energy and bevel angle were determined with the PTW microDiamond detector.

Additionally, OARs were assessed with the same detector, in both the crossline and inline directions for all these combinations, at three different depths: the depth of maximum dose (z_{max}), the 90% depth dose (R_{90}) and the 50% depth dose (R_{50}). For beveled applicators, the major axis was aligned along the crossline direction, and PDDs were obtained along the clinical axis, perpendicular to the water surface.

OFs were determined at the depth of z_{max} under the assumption that electron perturbation factors for the microDiamond detector remain constant for both inclined and flat applicators. Thus, Equation (1) was applied:

$$OF_{d,\alpha}^{meas} = \frac{M_{C_dB_\alpha}}{M_{C_{10}B_0}} \quad (1)$$

where $M_{C_dB_\alpha}$ represents the reading of the electrometer when the detector is positioned at z_{max} along the clinical axis of the C_dB_α applicator. Both readings in Equation (1) correspond to the same energy and monitor units.

The suitability of the microDiamond detector for IORT beams with mobile electron accelerators was already assessed in previous works.[16,21]

2.3 | Monte carlo simulation

Monte Carlo simulations were performed using penEasy 2020,[22] a general-purpose main program built on the PENELOPE 2018 Monte Carlo system,[23] which enables accurate modeling of coupled electron-photon transport. The penEasy framework provides modular support for defining particle sources, scoring absorbed dose distributions, and implementing variance-reduction techniques (VRTs). It allows flexible specification of beam models, tally geometries (Cartesian, cylindrical, or spherical), and energy spectra, including piecewise continuous and Gaussian-distributed spectra. penEasy supports both quadric-based and voxel-based geometries, or combinations of both.

In this study, the accelerator head and applicators were modeled using PENGEOM,[24] the native PENELOPE geometry module, which defines components as homogeneous bodies bounded by quadric surfaces. The geometry was built with the PenGeomJar

TABLE 2 Linac components and their source of information.

Component	Material	Source of information
Exit window (upper)	Titanium	Thickness (55 μm) from[a], position inspired by[b]
Cylindrical inner head	PEEK	Diameter optimized in this study; material from[c]
Scattering foil	Aluminum	Optimized thickness; material from[a]
Monitor ionization chambers	Aluminum	Arbitrarily placed, geometry inspired by[c]
Mylar exit window	Mylar	Optimized thickness; material from[a]
Applicator geometry	PMMA	Based on measurements
Applicator wall material	PMMA	Manufacturer-provided information

[a]Winkler et al.[20]
[b]Righi et al.[14]
[c]Iaccarino et al.[12]

graphical interface. The simulations were executed on a server equipped with 32 GB of RAM and two Intel Xeon E5-2695 v2 processors at 2.4 GHz, enabling parallel execution across 48 threads.

The initial geometry and materials were based on the previous model, Liac 12 MeV (S.I.T.), and were adapted to match the applicator length (40 cm) and the SSD of the new accelerator (64.5 cm). Following Winkler et al.,[20] the exit window of the accelerating waveguide is made of titanium and is 55 μm thick, while the scattering foil is composed of aluminium, though its exact thickness has not been disclosed.

In our model, the titanium window was positioned at $z = 66.14$ cm as a reasonable assumption based on the previous model,[14] given that its exact placement is not disclosed by the manufacturer. Two monitor ionization chambers were incorporated, each consisting of two aluminum foils, 5 μm thick, with a distance between walls of 100 μm. These chambers were placed arbitrarily within the linac head, with their top walls located at $z = 55.30$ and $z = 54.90$ cm. Due to their extremely thin structure, the monitor chambers are not visible in Figure 1.

The materials inside the head of the linac have been assumed to be the same as in the previous model, with PEEK used for the head structure and Mylar for the head exit window. To achieve optimized agreement with our measurements, only three geometric parameters were adjusted: the inner diameter of the head, the thickness of the scattering foil, and the thickness of the Mylar exit window. A summary of the linac head components included in the simulation, along with their materials and sources of information, is provided in Table 2.

The electron source was positioned at $z = 65$ cm (0.5 cm above the scattering foil) using the source box Isotropic Gauss Spectrum section in penEasy. It was modeled as a Gaussian source with a full width at half maximum (FWHM) of 0.025 cm in both the x and y directions, and embedded within a square box with a side length of 0.05 cm. The particle directions were confined within a cone with semi-aperture angle of 0.1° oriented along the $-z$ axis. To expedite the calculations, the source was placed below the titanium exit window. The scattering effects introduced by the window were indirectly accounted for by adjusting the three geometrical parameters previously described and optimizing the energy spectrum of the electron source.

The selection of these three geometrical parameters, together with the electron energy spectrum, for optimization was guided by their expected influence on key dosimetric characteristics, informed by previous work by Björk et al.[25]: the depth-dose distribution was anticipated to be primarily influenced by the initial electron energy spectrum; the linac head diameter was chosen due to its potential impact on the OFs; and the remaining two geometrical parameters (scattering foil thickness and Mylar window thickness) were included based on their expected substantial impact on the shape of the OARs. Other source characteristics, such as the beam's radial intensity distribution and angular divergence, were fixed given their expected minor influence on these distributions.

Finally, in order to compare with experimental data, a cylindrical virtual water phantom with a diameter of 30 cm was positioned directly beneath the applicator. Figure 1 shows a 2D view of the geometry and materials used in the simulation of the $C_{10}B_0$ and C_3B_0 applicators.

The transport parameters used in the simulations are listed in Table 3. Default penEasy values were used, except for DSMAX in thin materials, where the PENELOPE recommendation of selecting a value at least ten times smaller than the thickness of the material was followed.

Regarding the acquisition of data in the MC simulations, different penEasy tallies were used at various stages of this study and are detailed in their respective sections. The associated requested uncertainties correspond to the mean uncertainty of each bin within the respective tallies.

TABLE 3 Transport parameters for the materials used in penEasy simulations with the PENELOPE code. DSMAX values of 10^{30} signify that step-length control is essentially inactive for these materials, as adequate interactions take place without the need for this constraint. This is particularly relevant for materials present in relatively large volumes within the simulation geometry, where imposing a step-length limit is unnecessary.

Material	EABS (e^- and e^+) (eV)	EABS (ph) (eV)	C_1	C_2	W_{cc} (eV)	W_{cr} (eV)	DSMAX (cm)
Air (*)	10^5	10^4	0.1	0.1	$1.4{\cdot}10^5$	$1.4{\cdot}10^4$	10^{30}
Aluminium (Al)	10^5	10^4	0.1	0.1	$1.4{\cdot}10^5$	$1.4{\cdot}10^4$	10^{-4}
PEEK ($C_{19}H_{12}O_3$)	10^5	10^4	0.1	0.1	$1.4{\cdot}10^5$	$1.4{\cdot}10^4$	10^{30}
PMMA ($C_5O_2H_8$)	10^5	10^4	0.1	0.1	$1.4{\cdot}10^5$	$1.4{\cdot}10^4$	10^{-2}
Titanium (Ti)	10^5	10^4	0.1	0.1	$1.4{\cdot}10^5$	$1.4{\cdot}10^4$	10^{-4}
Water (H_2O)	10^5	10^4	0.1	0.1	$1.4{\cdot}10^5$	$1.4{\cdot}10^4$	10^{30}
RW3 (**)	10^5	10^4	0.1	0.1	$1.4{\cdot}10^5$	$1.4{\cdot}10^4$	10^{30}

*The composition of the Air material was defined using mass percentages with N (78.44%), O (21.07%), Ar (0.47%) and C (0.01%).
**The composition of the RW3 material was defined using mass percentages with C_8H_8 (98%) and TiO_2 (2%). RW3 was only used for validation with radiochromic film.
Abbreviation: PMMA, polymethyl methacrylate.

2.3.1 | Model optimization

We initially used the geometry and materials from the previous Liac 12 MeV model, as described in the preceding section. For the energy spectrum optimization, we adapted the methodology proposed by Iaccarino et al.,[12] which incorporates concepts from Zhengming and Jette[26] and Chvetson and Sandison.[27] Instead of performing monoenergetic simulations, we conducted simulations using small energy bins (ΔE_n), 47 bins from 4.0 to 13.2 MeV, each with a width of 0.2 MeV, plus an additional bin covering energies from 2.0 to 4.0 MeV. This approach resulted in a total of 48 simulations, matching the available computational threads on the server. Within each energy bin, electron energies were uniformly distributed across the bin's range.

The simulated applicators included $C_{10}B_0$, C_4B_0, and an additional geometry C_0, which represents the no-applicator setup. The $C_{10}B_0$ applicator was selected as it is the reference applicator, while the C_4B_0 applicator due to its maximum output factor observed during preliminary measurements. This choice allows us to assess agreement under conditions of maximum dose delivery, as the highest OF serves as an upper limit–if this combination meets the required agreement, other configurations are also expected to comply. The C_0 geometry was included to evaluate the accuracy of the MC model independently from applicator effects.

Energy spectrum optimization was performed by minimizing the quadratic differences at various depths z_i between the experimentally determined $PDD_d^{meas}(z_i)$ and the resulting $PDD_d^{MC}(z_i)$ from a linear combination of dose distributions simulated for small energy bins (Equation (2)). Similar minimization strategies have been proposed in previous works for conventional accelerators.[28,29]

$$D_d^{MC} = \sum_{n=1}^{48} w_n D_{d,\Delta E_n}^{MC} \tag{2}$$

where $D_{d,\Delta E_n}^{MC}$ represents the dose distribution calculated using an applicator of diameter d and the small energy bin ΔE_n, and D_d^{MC} refers to the resulting linear combination. The coefficients w_n were determined using Equation (3) through the Generalized Simulated Annealing algorithm,[30,31] as implemented in the SciPy Python package.[32]

$$\min \sum_{d=0,4,10} \left(\sum_{i=1}^{N} (PDD_d^{MC}(z_i) - PDD_d^{meas}(z_i))^2 \right) \tag{3}$$

where N is the total number of points z_i at which differences are computed.

Since finding the solution of Equation (2) that minimizes Equation (3) is an ill-posed problem with infinite solutions, bounds were applied during the minimization to ensure the results remained physically meaningful. Given that the linac lacks a bending magnet, the expected energy spectrum should consist of a peak at the high-energy end and a gradually increasing low-energy component.[12,26,27]

It is important to emphasize that while the linear combination from Equation (2) is performed on dose distributions ($D_{d,\Delta E_n}^{MC}$), the minimization in Equation (3) is applied using PDDs derived from the resulting dose distributions of the linear combination (D_d^{MC}).

For the remainder of the model optimization process, data were recorded using the Cylindrical Dose Distribution tally, taking advantage of the cylindrical symmetry of the problem. The grid size was set to 2 mm in both

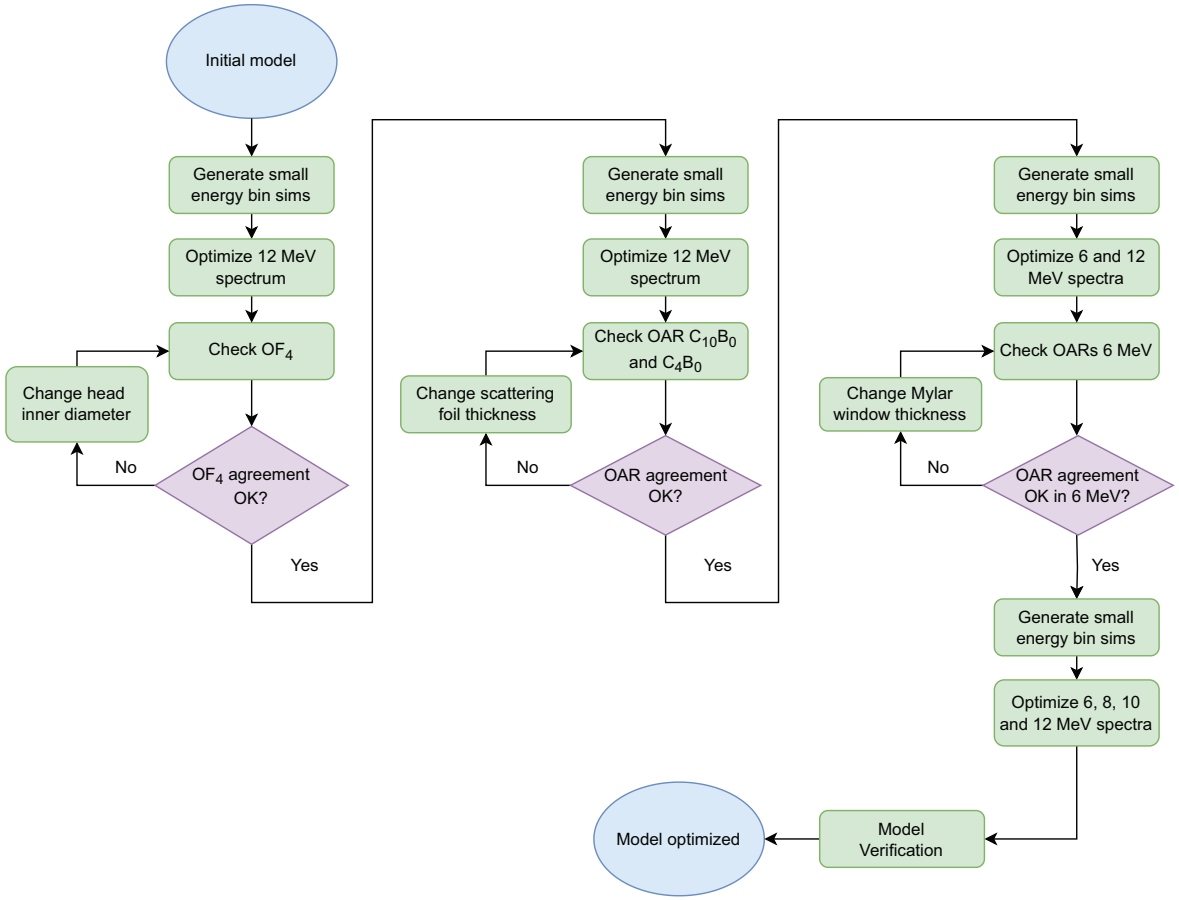

FIGURE 2 Workflow diagram illustrating the model optimization process for the Liac HWL MC simulations. In each optimization step, parameters are adjusted until the agreement with the corresponding experimental measurements is acceptable. Once a parameter achieves this level of agreement, it is kept fixed for all subsequent optimization steps. The measurements used for model optimization include PDDs of $C_{10}B_0$, C_4B_0, and C_0 applicators, OARs at z_{max} for $C_{10}B_0$ and C_4B_0, and the output factor the C_4B_0 applicator (OF_4 in the figure) for each energy. OARs, off-axis ratios; PDD, percentage depth dose.

radial and z directions. Simulations were stopped once an uncertainty of 1% ($k = 2$) was reached.

Spectrum optimization was repeated throughout the model optimization which is visually represented in Figure 2 and described in the following paragraphs.

We began by optimizing the spectrum for the 12 MeV beam, followed by verifying the OF for the C_4B_0 applicator. To achieve the best agreement with measurements, we adjusted the inner diameter of the accelerator's cylindrical head in 0.25 cm increments, ranging from 2 to 4.5 cm, and selected the diameter that provided the closest match.

Subsequently, we re-ran the simulations for the different energy bins with the updated head diameter for the C_4B_0 and $C_{10}B_0$ applicators and re-optimized the 12 MeV energy spectrum. We then evaluated the OARs. If discrepancies were found, we adjusted the scattering foil thickness and repeated the process until acceptable agreement was reached.

After refining the 12 MeV beam, we proceeded to optimize the 6 MeV beam. During this stage, we observed horns near the edges of the applicator in the 6 MeV simulations that did not match the measurements. To address this, we modified the thickness of the Mylar exit window. Once suitable agreement was obtained, we re-simulated the energy bins with the updated geometry and optimized the energy spectra for 6, 8, 10, and 12 MeV.

Finally, we evaluated the OF for the C_4B_0 applicator, as well as the OARs and PDDs of $C_{10}B_0$ and C_4B_0, against the measured values to ensure that they met the desired agreement criteria.

2.3.2 | Gamma analysis of PDDs and OARs

To assess the agreement between MC-calculated and measured PDDs and OARs, a global gamma analysis[33] was conducted using the PyMedPhys package (v. 0.39.2),[34] with a criterion of 2% dose difference and 1 mm distance-to-agreement criteria. For PDD comparisons, dose normalization was set to the maximum measured dose, while for OAR comparisons, normalization was performed at $x = 0$. The implementation of the gamma analysis included interpolation of the calculated

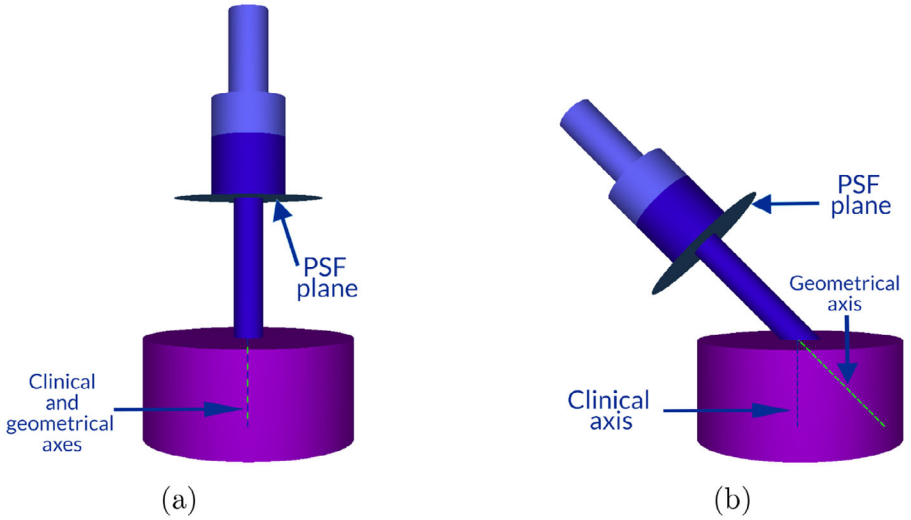

FIGURE 3 Pengeomjar 3D view of the simulated geometry of the Liac HWL with the C_5B_0 (a) and C_5B_{45} (b) applicators. The disc below the bevel junction represents the spatial region where particles in the PSFs were recorded. Dashed lines denote the clinical and geometrical axes. PSFs, phase-space files.

grid, generating data points every 0.2 mm to ensure adequate resolution for the selected criteria.[35] A point was considered to pass if the gamma value was less than or equal to 1. Hereafter, we refer to this as the 2%, 1 mm gamma analysis.

A PDD or OAR profile was considered to fulfill the passing rate (PR) threshold if at least 90% of its points satisfied the gamma criterion, in line with commonly used tolerance levels in the literature. Although profiles with slightly lower PRs may still exhibit acceptable overall agreement, the 90% threshold was selected as a practical benchmark for consistency and comparison across different configurations.

2.3.3 | Calculation of dose distributions

Dose distributions were calculated using a two-step process. First, for each applicator diameter and energy, the flat applicator was simulated, and a PSF was recorded just below the bevel junction (Figure 3) using the PhaseSpace File tally. The generated PSF was then used to simulate the four bevel endings, with the PSF rotated according to the bevel angle. Due to the lack of cylindrical symmetry in beveled applicators, the Spatial Dose Distribution tally was used instead of the Cylindrical Dose Distribution to record the resulting dose distributions in the central region of the cylindrical water phantom, using a 2 mm grid resolution. Simulations were run until a statistical uncertainty of 0.5% ($k = 2$) was achieved.

2.3.4 | OF determination

For the determination of OFs from the MC simulations, we used the Cylindrical Dose Distribution tally with a disc of radius 1.5 mm and a height of 0.1 mm, centered at the depth of z_{max} for each combination of energy, applicator diameter, and bevel ending. This small thickness was chosen to address the issue of volume averaging, particularly for inclined applicators, where isodoses are compressed in the depth direction.[16] As in the previous section, the required statistical uncertainty was set to 0.5% ($k = 2$).

The OFs were determined as the ratio of the absorbed dose per history calculated at z_{max} from the simulation of an applicator with diameter d and bevel angle α, to the absorbed dose per history calculated for the reference applicator $C_{10}B_0$ at the same energy (Equation (4)).

$$OF_{d,\alpha}^{MC} = \frac{D_{C_dB_\alpha}}{D_{C_{10}B_0}} \tag{4}$$

2.3.5 | Computational time

A study of computational time was performed to provide an estimate of the time required for model optimization (including parameter adjustments), PSF generation and determination of absorbed dose distributions.

2.3.6 | Validation

Validation of the model was performed by comparing the computed and measured OFs, PDDs, and OARs for applicator and energy combinations that were not used during model optimization. Specifically, $C_{10}B_0$ and C_4B_0, which were employed to refine the model parameters, were excluded from

validation. Instead, a separate set of applicators was used to independently assess the accuracy of the final model.

Additionally, further validation was performed by comparing a computed 2D dose distribution with measurements obtained using Gafchromic EBT4 radiochromic film. The film was calibrated following the triple-channel calibration method described by Micke et al.[36] and was embedded in 30x30 cm^2 RW3 slabs instead of a water phantom. The MC absorbed dose distribution was obtained following the same methodology as in the calculation of dose distributions in water, replacing the water material with RW3. The same gamma analysis was applied as before, but in two dimensions. In this case, the dose normalization was performed at $x,y = 0$, and a low-dose cutoff was introduced, analyzing only points where the measured absorbed dose was at least 10% of the normalization value. To incorporate absolute dose differences and address the limitations of relative profile comparisons, both dose distributions in this 2D analysis were scaled by their respective OFs at the central axis: the measured film data by the experimentally determined OF, and the MC dose by the corresponding simulated OF. This allowed the evaluation to reflect both spatial and absolute dose agreement in a clinically relevant scenario.

3 | RESULTS

3.1 | Model optimization

3.1.1 | Influence of the head inner diameter

The impact of the cylindrical accelerator head's inner diameter on the OF was evaluated for the 4 cm applicator. As shown in Figure 4, the OF exhibits a noticeable variation as the head diameter changes. The best agreement with the measured OF was achieved with a head diameter of 4 cm (<1%). Geometries with a head inner diameter larger than 4 cm were dismissed, as they inevitably resulted in reduced fluence due to partial obstruction of the electron beam by the 4 cm aperture at the head exit window.

3.1.2 | Influence of the scattering foil thickness

Figure 5 illustrates the effect of modifying the scattering foil thickness on OARs. The impact is notable for the $C_{10}B_0$ applicator, while it remains minimal for C_4B_0. A thickness of 610 μm was found to provide the best agreement with the measurements.

3.1.3 | Influence of the exit window thickness

The influence of the Mylar exit window thickness on OARs is demonstrated in Figure 6. An optimal thickness of 350 μm was identified through comparison with experimental data. Increasing the thickness beyond this value does not improve agreement and would not be realistic, as the increased attenuation of the material would lead to a reduction in dose per pulse.

3.1.4 | Final spectrum optimization and model verification

The model was optimized with a head inner diameter of 4 cm, a scattering foil thickness of 610 μm, and a Mylar exit window thickness of 350 μm. The resulting initial spectra incident on the aluminum scattering foil are shown in Figure 7, while the corresponding PDDs and OARs from the optimization process are presented in Figures 8 and 9, respectively. All PDD comparisons yielded gamma PRs greater than 95%. Additionally, all points for the $C_{10}B_0$ and C_4B_0 applicators OARs meet the gamma criterion, with the exception of the C_4B_0 at 6 MeV where deviations occur near the applicator wall.

Notably, once the inner diameter of the head was fixed, the output factor of the C_4B_0 applicator at 12 MeV varied by less than 1% throughout the optimization process.

3.2 | Validation

Given the large number of combinations of energy, applicator diameter, and bevel angle, only a representative subset of PDDs and OARs is compared in the following sections. OFs, however, are presented in detail due to their direct relevance to treatment planning in IOERT. Additionally, a 2D verification using radiochromic film was performed for the specific case of the 12 MeV beam using a large-diameter applicator with the maximum bevel angle ($C_{10}B_{45}$) at z_{max}, as described in the corresponding subsection.

3.2.1 | PDDs

Figure 10 compares MC-calculated and measured PDDs for a representative set of applicator configurations, covering a range of diameters and bevel angles. The selection includes the largest and smallest applicator diameters, the steepest bevel angles ($C_{12}B_{45}$ and C_3B_{45}), flat-end applicators ($C_{12}B_0$ and C_3B_0), and intermediate cases (C_6B_{15} and C_6B_{30}). The gamma analysis shows a PR above 95% for all comparisons.

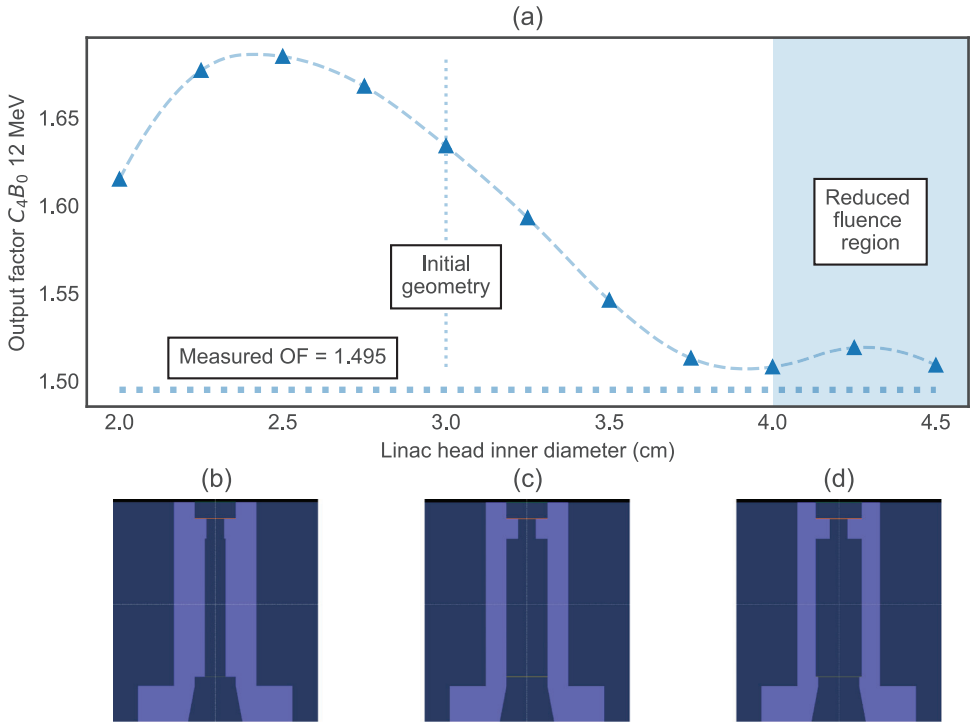

FIGURE 4 (a) Variation of the OF of the C_4B_0 applicator as a function of the inner diameter of the linac head for the 12 MeV beam, with the dashed line representing a quadratic interpolation. The optimization was performed with steps of 0.25 cm, providing satisfactory agreement with the measured data. Further refinement of the inner diameter is possible, but would require more computational resources. (b–d) Geometry of the linac head for different inner diameters: (b) 2 cm, (c) 4 cm, and (d) 4.5 cm. In (d), the larger inner diameter results in a reduction in fluence, as the head exit window measures 4 cm in diameter, causing the excess portion to act as a passive collimator. OF, output factor.

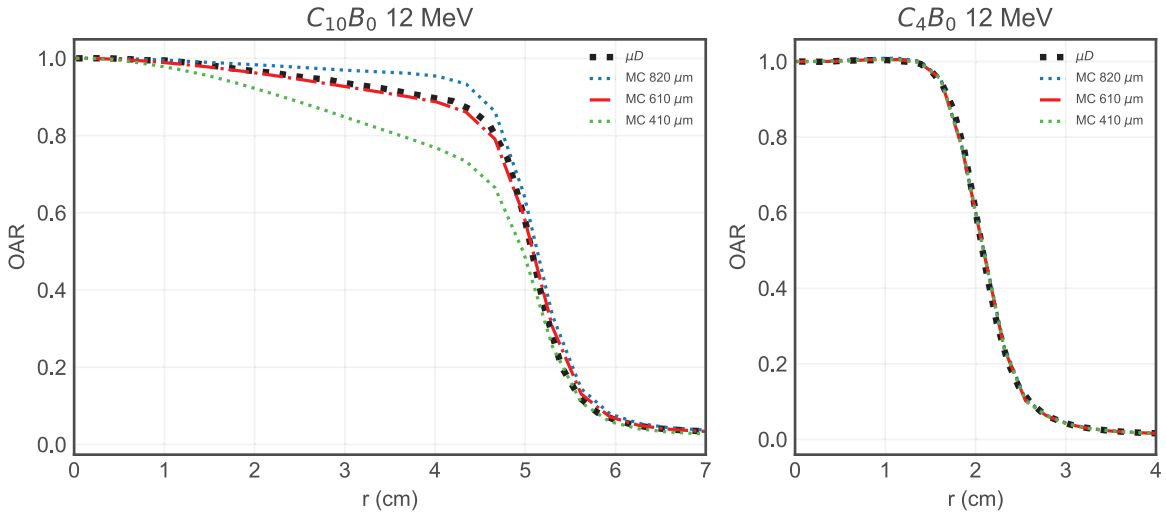

FIGURE 5 OARs at z_{max} vs scattering foil thickness for the 12 MeV beam and applicators $C_{10}B_0$ and C_4B_0. μD in the legend refers to OARs measured experimentally with a microDiamond detector, and MC stands for MC–calculated OARs. For $C_{10}B_0$, the shape of the OARs is strongly influenced by the scattering foil thickness, while for C_4B_0, the effect is minimal and goes largely unnoticed. OARs, off axis ratios.

3.2.2 | OARs

Figures 11 and 12 compare OARs for different energies and applicator configurations at three relevant depths: z_{max}, R_{90}, and R_{50}. Figure 11 presents the results for flat applicators, while Figure 12 includes selected configurations with different bevel angles, showcasing both the most challenging cases ($C_{12}B_{45}$ and C_3B_{45}) and other configurations (C_6B_{15} and C_6B_{30}) for comparison. For flat applicators, all points pass the gamma criterion

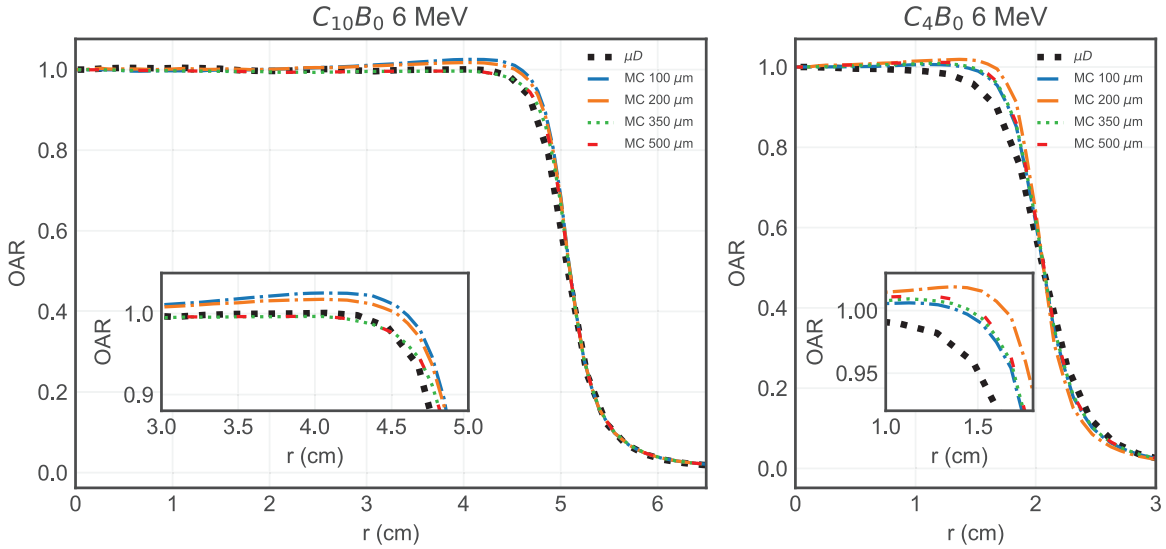

FIGURE 6 Measured (μD) and simulated (MC) $C_{10}B_0$ and C_4B_0, 6 MeV, OARs at z_{max} for different Mylar exit window thicknesses (100, 200, 350, and 500 μm). The inset highlights subtle changes in the OAR profiles in the region of interest. OAR, off axis ratio.

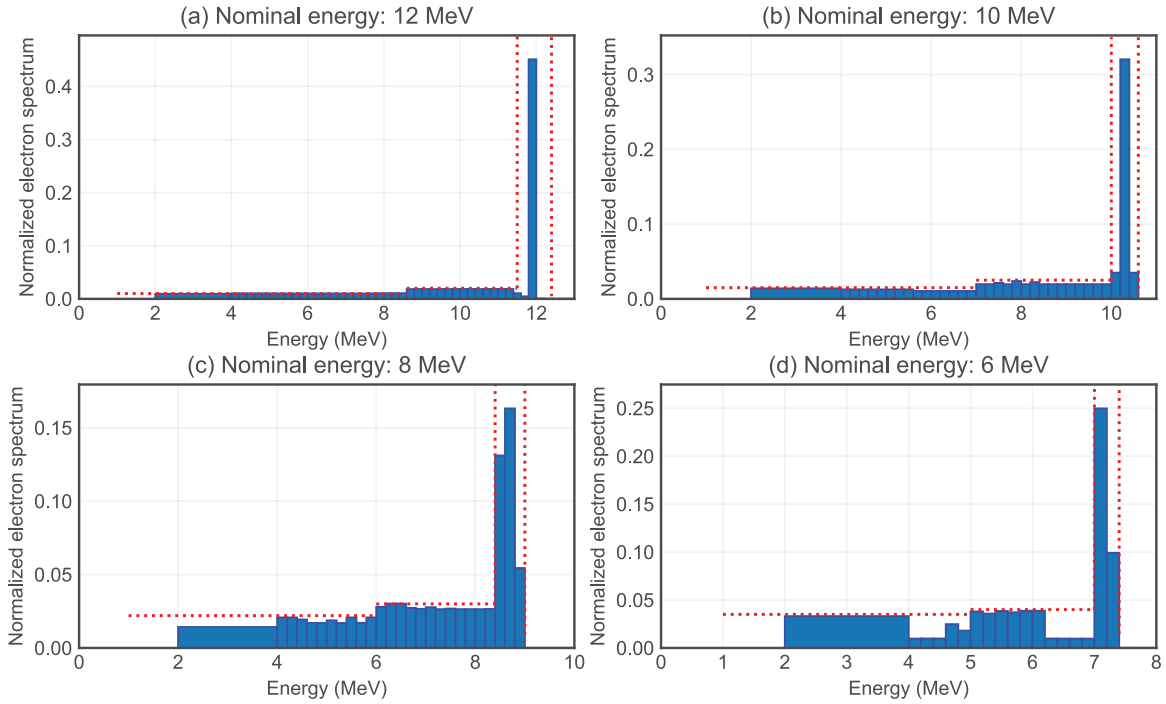

FIGURE 7 Optimized spectra for the four nominal energies (12, 10, 8, and 6 MeV), with the bounds of the optimization process indicated by red dotted lines. The bounds are divided into three regions: one below two-thirds of the beam maximum energy, another from two-thirds of the maximum energy to the peak, where the bounds are higher to account for an increasing contribution in the low-energy region, and a final region corresponding to the peak, where no bounds were applied.

except for the $C_{12}B_0$ and C_3B_0 at 6 MeV in the OAR at z_{max} near the applicator wall. For beveled applicators, the gamma analysis shows the largest deviations near the applicator walls at z_{max} of the $C_{12}B_{45}$ combinations, and particularly pronounced deviations for the C_3B_{45} combinations near the positive-side applicator wall, with PRs below 90%.

3.2.3 | Radiochromic film verification

Figure 13 compares the $z = z_{max}$ dose plane measured with radiochromic film embedded in RW3 slabs, for the $C_{10}B_{45}$ applicator at 12 MeV, with the corresponding MC-calculated dose plane. The gamma analysis with the 2%, 1 mm criterion resulted in a PR slightly below

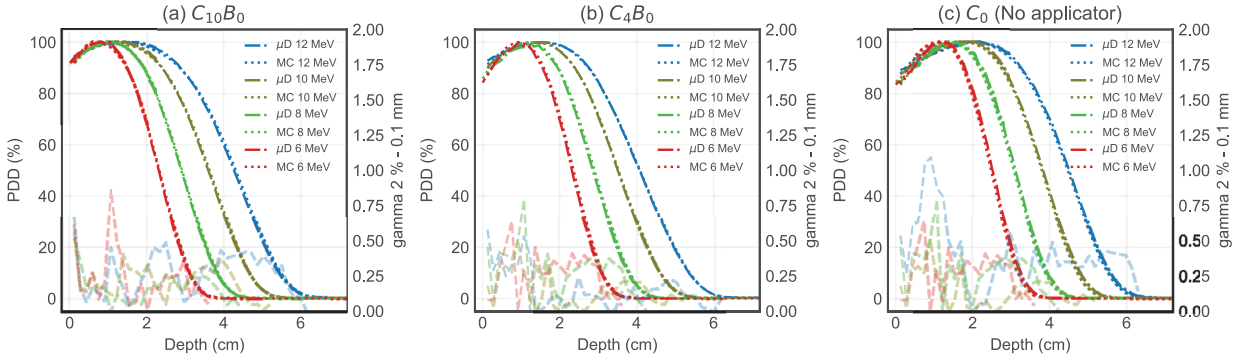

FIGURE 8 Measured (μD) and MC-calculated (MC) PDDs for the nominal energies 12, 10, 8, and 6 MeV are shown for the $C_{10}B_0$ (a), C_4B_0 (b), and no applicator (C_0) (c) configurations used in model optimization. The agreement with the MC model is compared across the three setups. Different colors represent different nominal energies in the PDDs and gamma analysis. All PDD comparisons have a gamma PR above 95%. PDD, percentage depth doses; PR, passing rate.

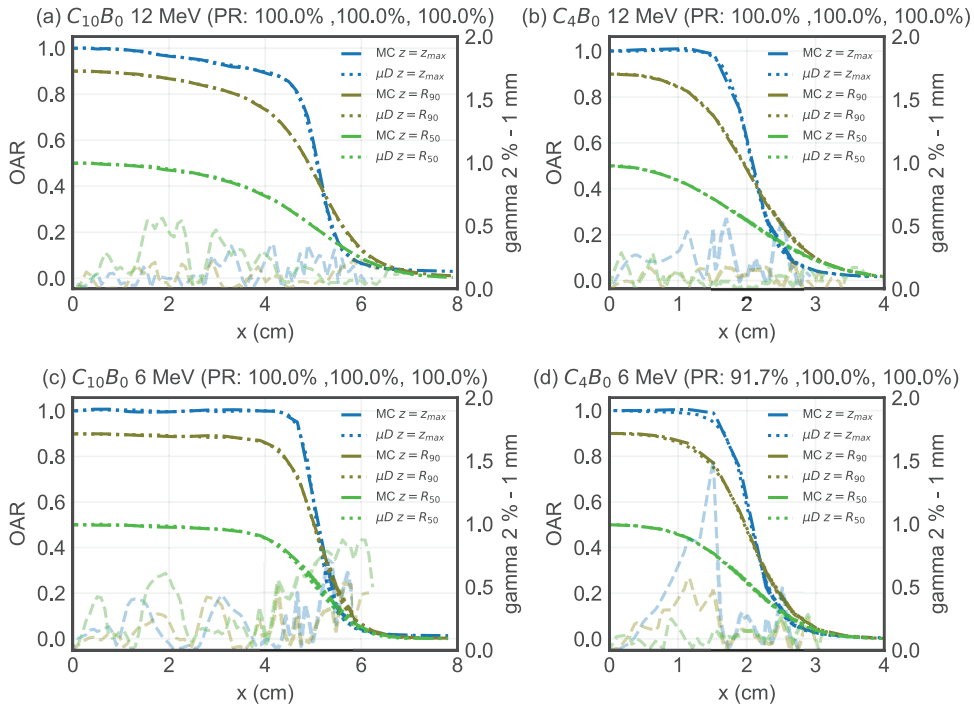

FIGURE 9 Comparison of symmetrized measurements (μD) and penEasy-calculated (MC) OARs in water for the $C_{10}B_0$ and C_4B_0 applicators, which were used during the optimization of the MC model. A 2%, 1 mm gamma analysis is overlaid, with PR indicated in the title of each subfigure. Different colors represent various depths in the OARs and gamma analysis. All points pass the gamma criterion except for the OAR at z_{max} for the C_4B_0 and 6 MeV combination, where the PR is 91.7%. OARs, off-axis ratios; PR, passing rates

the 90% threshold, primarily due to minor discrepancies near high-dose gradients and applicator edges. Therefore, an additional gamma analysis using a more relaxed 2%, 2 mm criterion was performed, showing a PR of 98.9%.

3.2.4 | OFs

A comprehensive comparison of experimentally determined and calculated OFs is presented in Figure 14 as well as Tables A1, A2, A3 and A4 of the Appendix section. A maximum difference of 1.7% was observed for flat applicators, while a maximum difference of 2.5% was found for beveled applicators.

3.3 | PSF analysis

In Figure 15, we present the electron and photon fluence versus radial distance, as well as the mean energy versus radial distance, for the 12 MeV PSFs of the $C_{10}B_0$

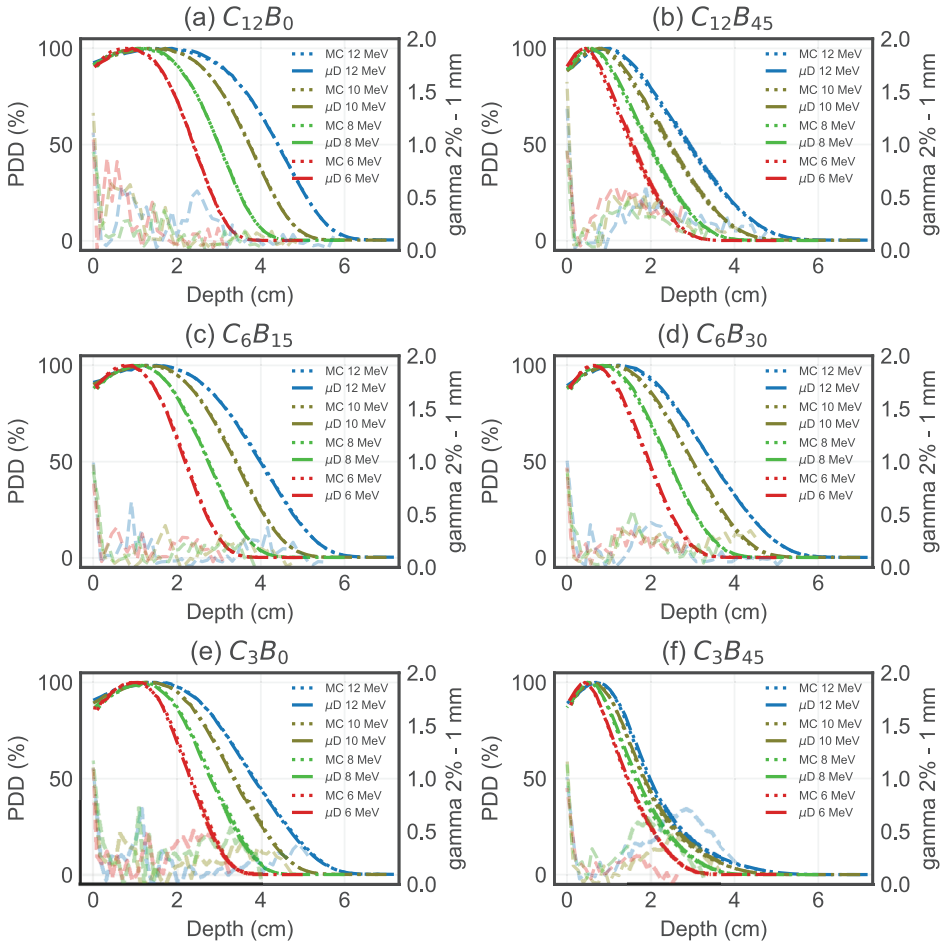

FIGURE 10 MC-calculated PDDs (MC) compared to measured ones (μD) for a selection of applicator combinations, including the largest and smallest applicator diameters, the highest bevel angles (b and f), and the flat endings (a and e), as well as intermediate cases (c and d). Different colors represent different nominal energies in the PDDs and gamma analysis. All PDD comparisons have a gamma PR above 95%. PDD, percentage depth doses; PR, passing rate.

and C_3B_0 applicators. For the $C_{10}B_0$ applicator, the electron fluence gradually decreases from the central axis ($r = 0$) until reaching the applicator wall at $r = 5$ cm. In contrast, the C_3B_0 applicator exhibits an increase in electron fluence near the applicator wall at $r = 1.5$ cm. The photon fluence shows an important contribution in the outer region (r >2 cm) for the C_3B_0 applicator, whereas it remains minimal outside the $C_{10}B_0$ applicator (r >5.5 cm).

When analyzing electron mean energy within the applicator, it is notably lower for the C_3B_0 applicator compared to the $C_{10}B_0$, due to increased scattering in the PMMA walls of the smaller applicator. Outside the applicator, the electron mean energy is higher for the smaller applicator (C_3B_0). The photon mean energy remains below 1 MeV in both cases, gradually increasing near the outer wall of the applicator before decreasing again with radial distance.

The PSFs generated in this study have been made publicly available on Zenodo.[37]

3.4 | Analysis of absorbed dose distributions

The results of absorbed dose distributions are presented for various combinations of applicators and electron energies. Figure 16 displays six different dose distributions, each selected to provide an overall understanding of the dosimetric properties of the beams. Most combinations exhibit homogeneous dose distributions, with high doses near the water surface (approximately 90%). However, it is evident that for higher energies and larger diameter applicators, the 90% isodose becomes relatively small.

3.5 | Computational time

The MC simulations required for model optimization and validation involved varying computational demands depending on the specific task. The simulation of small

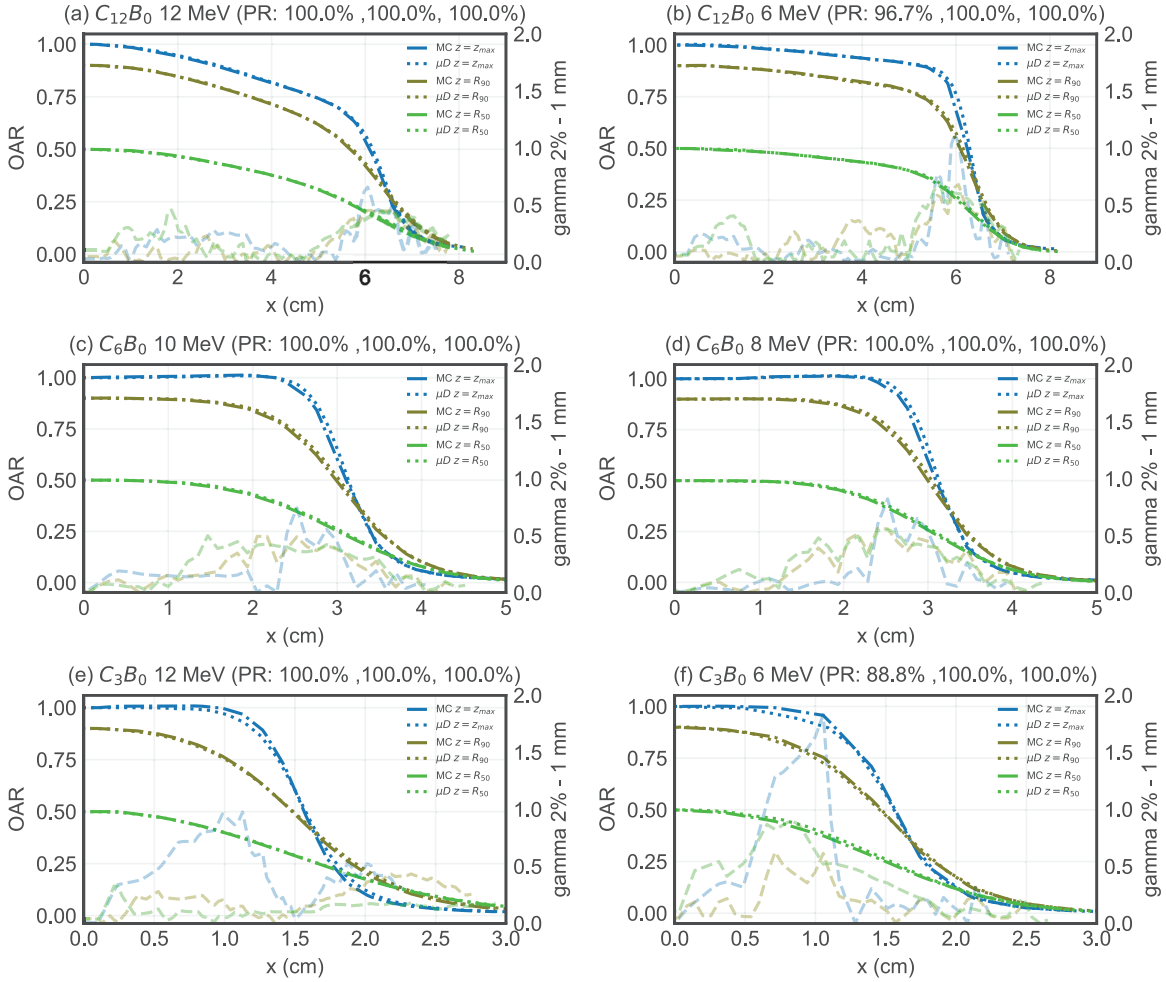

FIGURE 11 Comparison between symmetrized measurements (μD) and penEasy-calculated (MC) OARs in water for the $C_{12}B_0$, C_6B_0 and C_3B_0 applicators. A 2%, 1 mm gamma analysis is overlaid, with PRs (PR) indicated in the title of each subfigure. Different colors represent various depths in the OARs and gamma analysis. OARs, off axis ratios; PRs, passing rate.

energy bins, necessary for determining the initial energy spectrum, required approximately 18 h. For each modification of a single model parameter, the corresponding simulation took approximately 2 h. Given that the model optimization process involved tuning three parameters with at least three different values each (Figure 2), the total computational time for this stage amounted to approximately 102 h.

For PSF generation, where 4×10^7 particles were recorded, simulation times varied between 1 and 2 h, depending on the nominal beam energy (beams with low-energy electrons, which on average undergo more interactions before reaching the PSF scoring plane, lead to longer simulation times compared to higher-energy electron beams.). The same simulation runs were used to obtain both absolute dose distributions and OFs for all applicator, bevel, and energy combinations, with run times ranging from 3 to 3.5 h, again depending on the nominal energy simulated.

All computational times refer to the hardware configuration described previously in the Materials and Methods section.

4 | DISCUSSION

This work demonstrates how to effectively model a Liac HWL electron mobile accelerator for IORT without complete knowledge of the head geometry. The parameters adjusted include the linac head diameter, the scattering foil thickness, the head exit window thickness, and the beam's initial energy spectrum, each having a direct impact on simulation results. It has been shown that these parameters can be treated as independent, with each one predominantly influencing specific aspects of the output.

The linac head diameter primarily affects OFs, the scattering foil thickness influences the shape of the

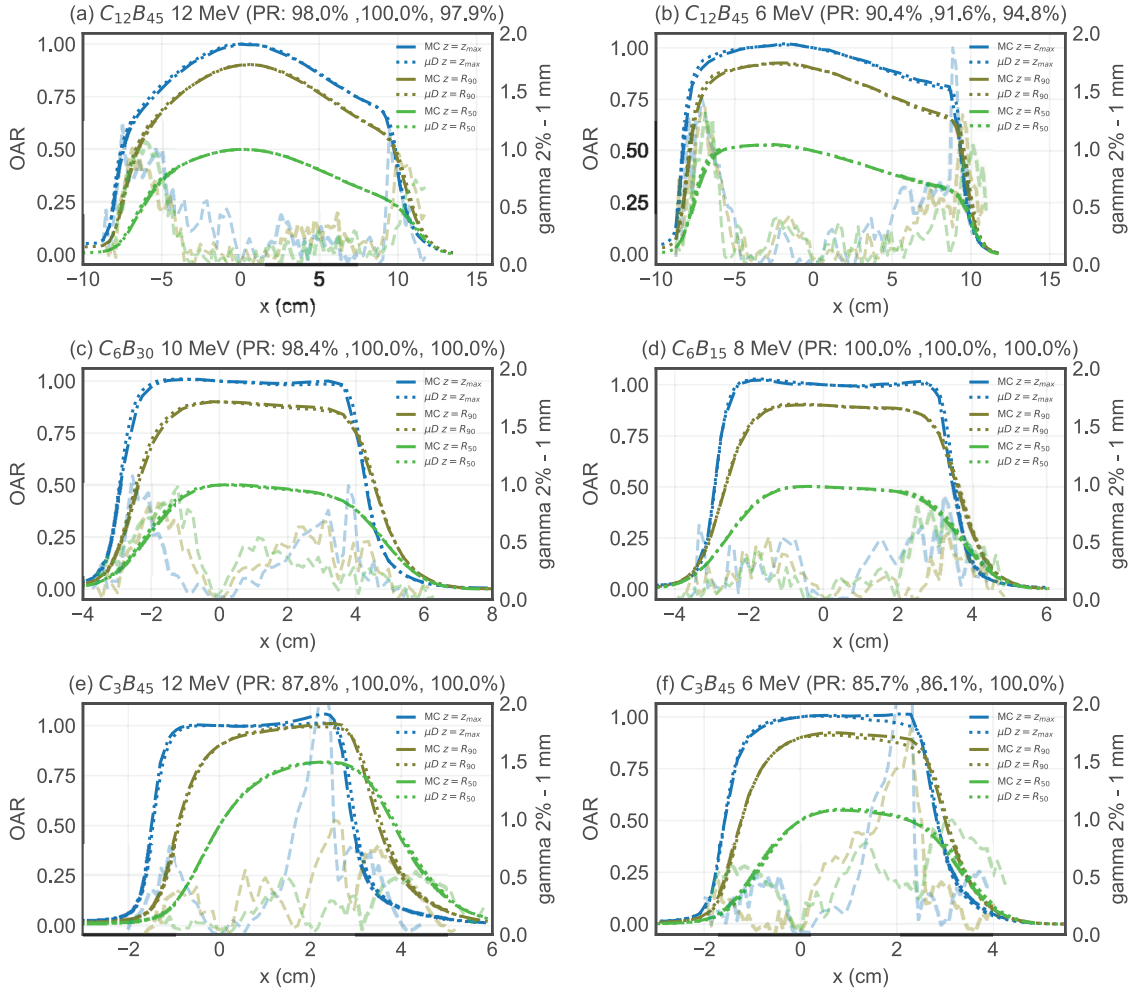

FIGURE 12 Comparison between measured (μD) and penEasy-calculated (MC) OARs in water for a selection of beveled applicators. A gamma analysis (2%, 1 mm) is overlaid with PR indicated in the title of each subfigure, ordered by increasing OAR depth. Different colors represent various depths in the OARs and gamma analysis. OARs, of axis-ratios, PR, passing rate.

OARs, the head exit window thickness impacts OARs at low energies near the beam edge, and the energy spectrum has a pronounced influence on the PDDs.

Despite relying on hypothetical parameters, the model developed with the parameters selected in this work demonstrates reasonable agreement with experimental data. OFs match the measurements with a maximum difference of 2.5%, and PDDs and OARs meet the 2%/1 mm gamma criterion, except for OARs with small-diameter applicators at shallow depths and low energies. This may be attributed to limitations in the modeled applicator geometry, where the actual rounded edges of the applicators are approximated by squared endings. This simplification arises because such geometries cannot be replicated using quadrics. It is important to note that current practice guidelines,[38,39] recommend a more relaxed criterion of 3% dose difference and 3 mm distance-to-agreement. Additionally, a 2D verification using radiochromic film provided further confirmation of the model's reliability, yielding a gamma PR close to 90% with the 2%, 1 mm criterion. A slightly lower PR compared to the profile-based comparisons could be anticipated, given the increased uncertainty associated with radiochromic film measurements due to their calibration and reading processes.

The limitations of the model, however, do not diminish its value as a reference to assist during the commissioning of new units. The model also provides insights into dose distributions across different applicators, helping users better understand the effects of varying nominal energies, applicator diameters and bevel angles. Throughout this study, we have been able to cover a wide range of results by adjusting the simulation parameters, demonstrating the model's flexibility in adapting to different conditions. Although the study was performed with applicator Set 2, applicator Set 1 only differs in the outer parts of the junctions between the head and the applicator and between the two parts of the applicator. Repeating the modeling process described in this study with the updated geometry should yield consistent results.

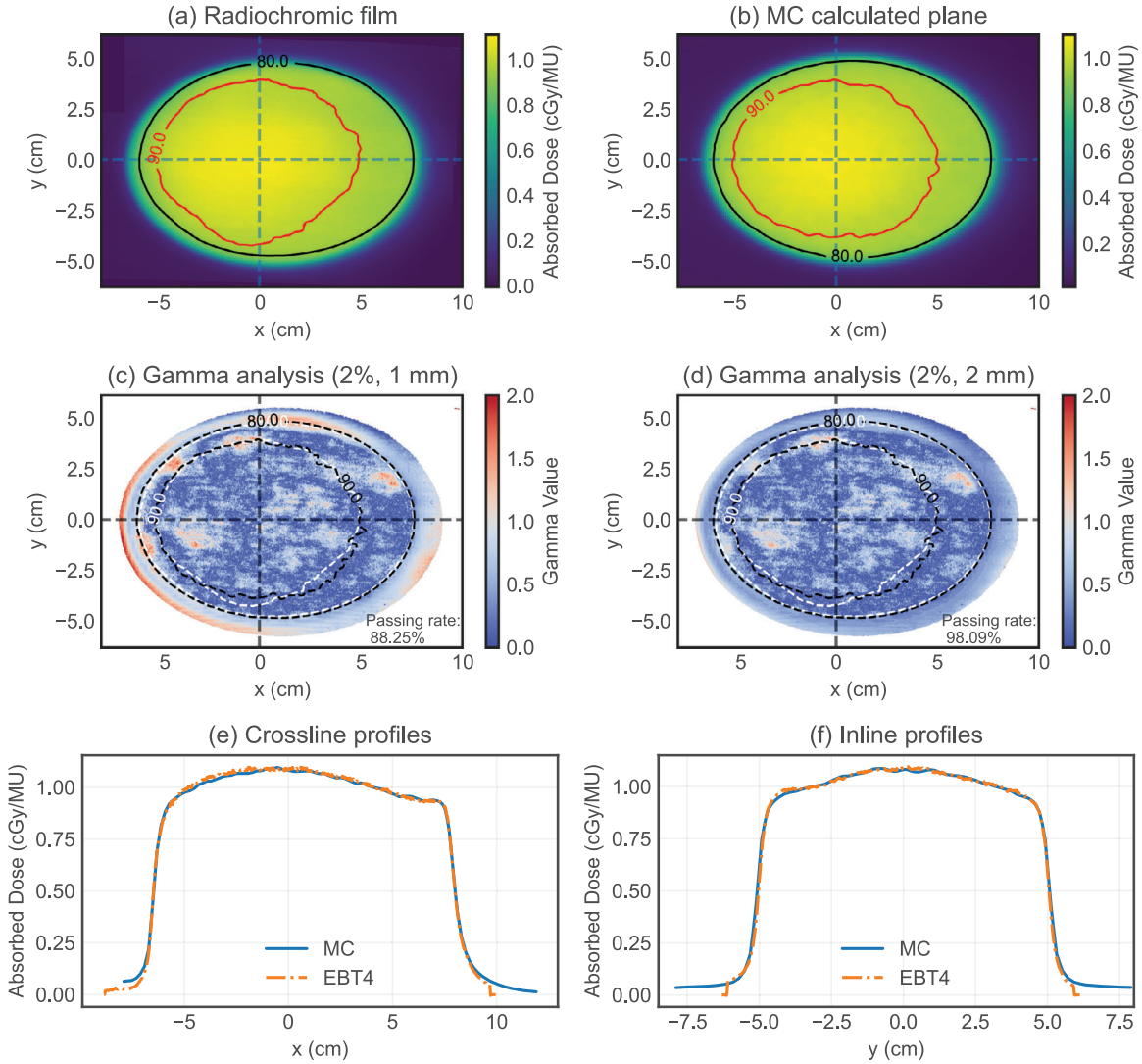

FIGURE 13 Comparison between measured and MC-calculated 2D dose distributions at z_{max} in RW3 for the 12 MeV beam using the $C_{10}B_{45}$ applicator. Each dose plane–measured and calculated–was scaled using its corresponding OF for enabling absolute dose comparison. Subfigures (a) and (b) show the absorbed dose distributions in cGy per monitor unit (cGy/MU) obtained from radiochromic film measurement and MC simulation, respectively. Subfigures (c) and (d) display gamma analysis maps evaluated with criteria of 2%, 1 mm and 2%, 2 mm, respectively. Due to the PR being slightly below the 90% threshold for the stricter 2%, 1 mm criterion, an additional gamma analysis using a more relaxed 2%, 2 mm criterion was performed to further investigate the agreement between measured and simulated dose distributions. Subfigures (e) and (f) present crossline and inline OARs comparing calculated (MC) and measured (EBT4) values. OARs, off axis ratios.

Beyond validating the model's dosimetric accuracy, this work also underscores its practical clinical value. The availability of MC-calculated dose distributions in water for various applicator geometries and energies supports informed decision-making during IOERT procedures, particularly when selecting the appropriate beam energy and applicator configuration. For example, understanding the behavior of the 90% isodose line with respect to bevel angle and applicator diameter can help anticipate and mitigate underdosing at the target periphery or overdosing of adjacent healthy tissues. These visualizations serve as an intuitive and clinically useful resource for radiation oncologists and medical physicists during intraoperative planning.

Moreover, the visualization of absorbed dose distributions from large diameter applicators has proven useful in identifying potential dosimetric deficiencies. It is ultimately a clinical decision whether certain combinations of applicator and energy need to be rescaled to deliver the desired dose to the target. In some cases, the level of heterogeneity in the dose distribution may be so pronounced that rescaling could introduce unacceptable hotspots, rendering those combinations clinically unsuitable. The issue of decreased homogeneity with large applicators and high energies has been previously identified by Oliver et al.,[40] where a proof-of-concept for an additional flattening filter was described as a potential solution. Additionally, this problem can

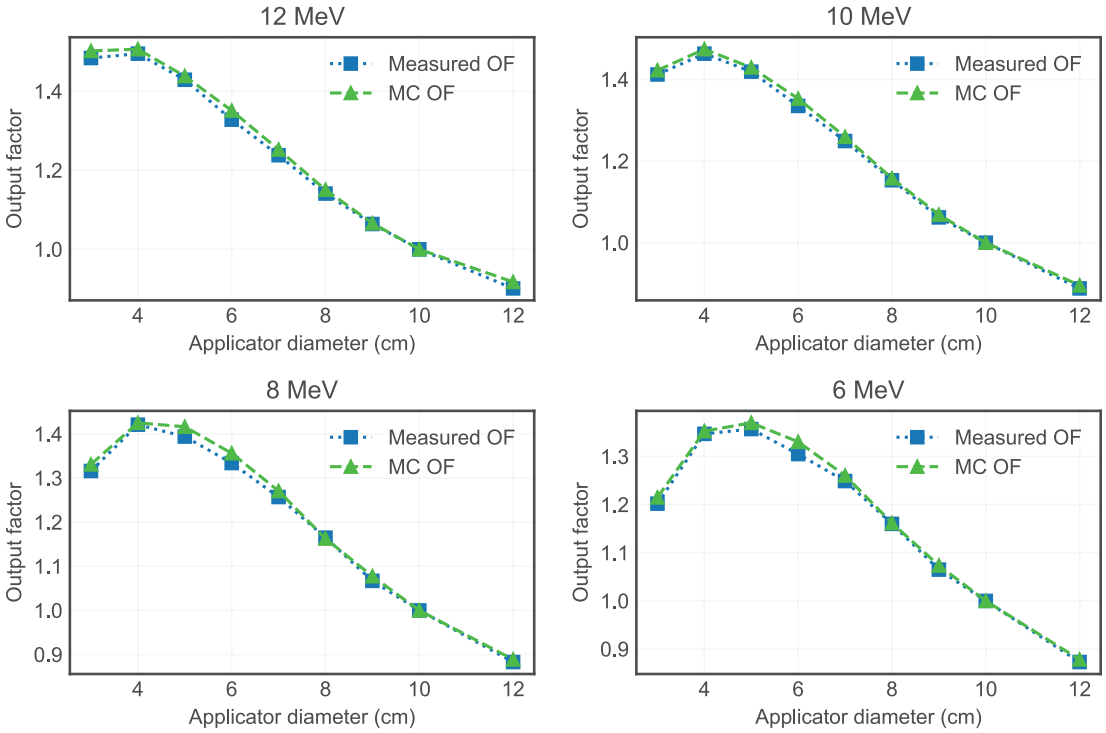

FIGURE 14 Comparison of measured and MC-calculated OFs for the four nominal energies with flat applicators. A maximum difference of 1.7% is observed. OFs, output factors

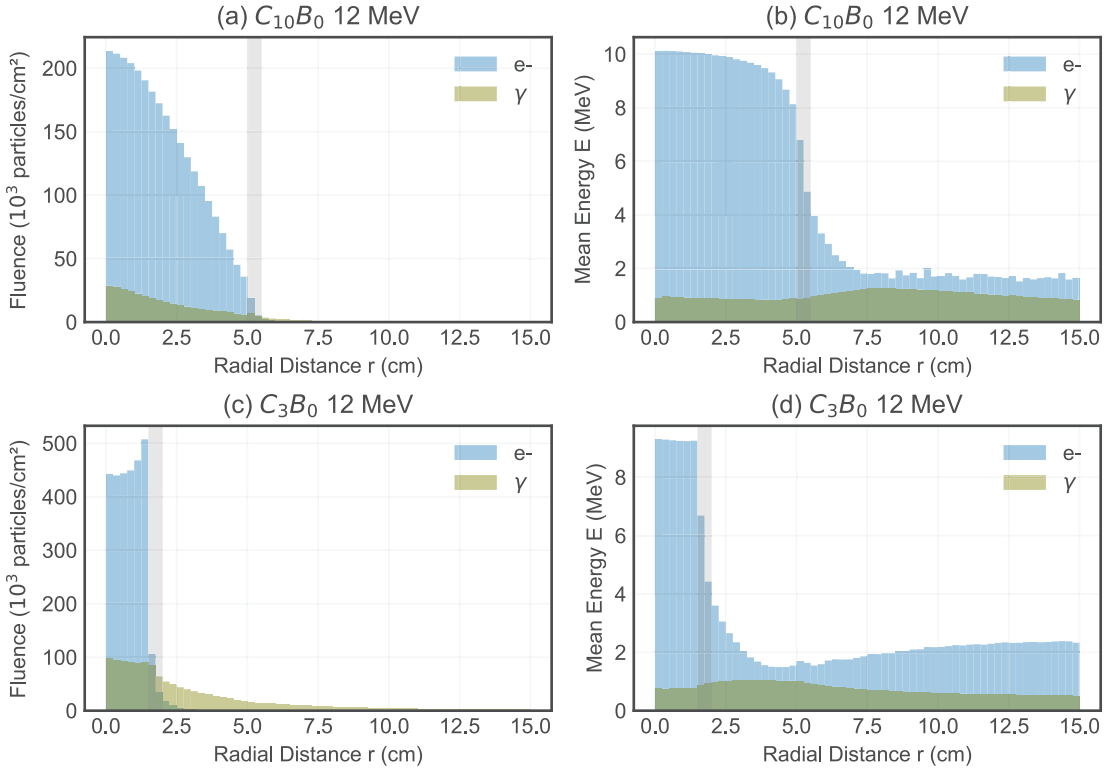

FIGURE 15 Radial distribution of electron (e-) and photon (γ) fluence and mean energy for the 12 MeV PSFs (N = 10^6) of the $C_{10}B_0$ and C_3B_0 applicators. The applicator wall is indicated in gray. (a) Electron and photon fluence versus radial distance (r) for the $C_{10}B_0$ applicator, showing a gradual decrease in electron fluence until reaching the applicator wall. (b) Mean energy versus r for the $C_{10}B_0$ applicator, illustrating the energy distribution within and outside the applicator. (c) Fluence versus r for the C_3B_0 applicator, where an increase in electron fluence is observed near the applicator wall. (d) Mean energy versus r for the C_3B_0 applicator, highlighting the lower electron mean energy within the applicator and higher energy outside when comparing to the $C_{10}B_0$ applicator. PSFs, phase space files.

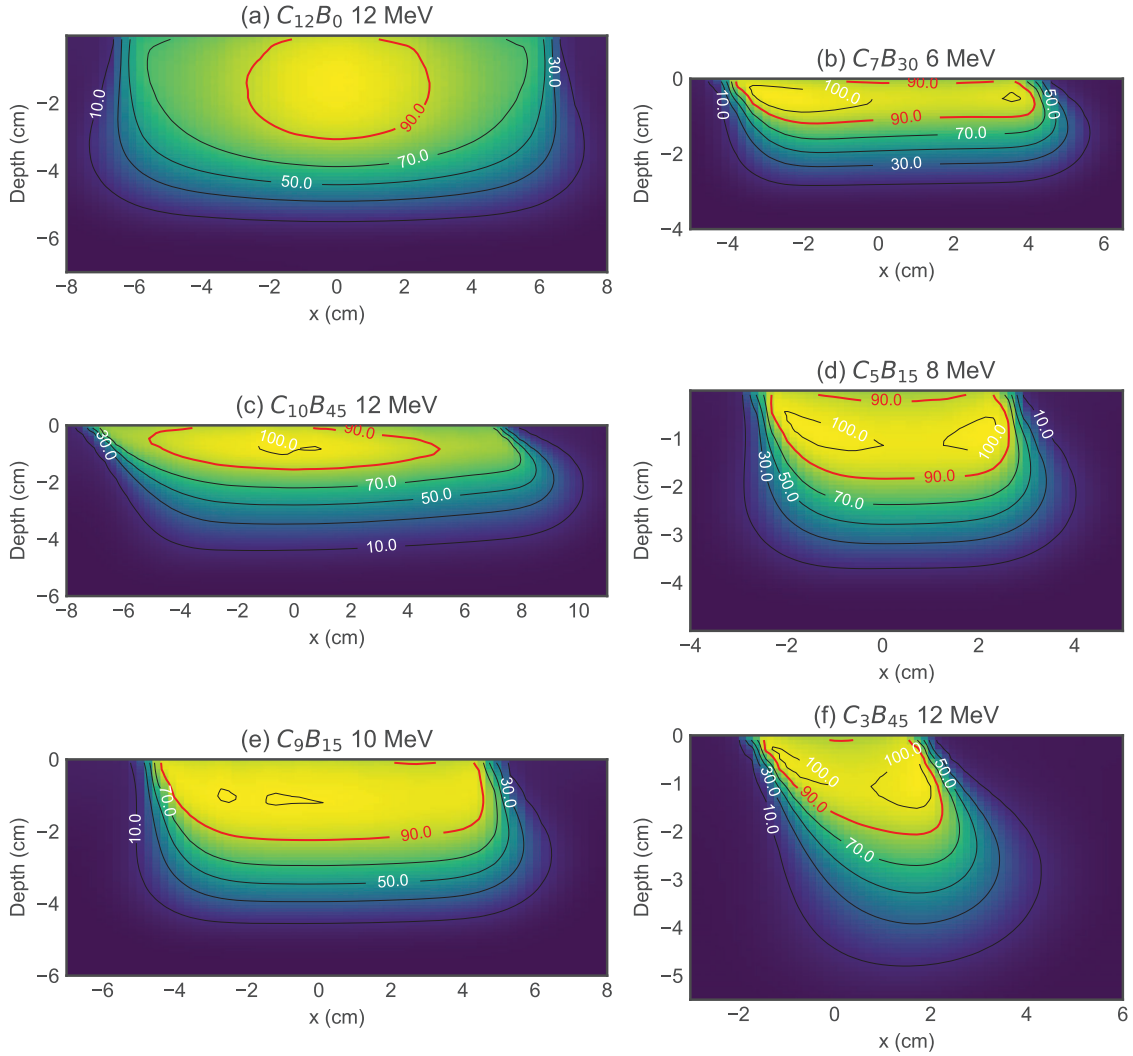

FIGURE 16 2D dose planes in the crossplane direction at $y = 0$ cm for six different combinations of applicators and electron energies. Several isodose levels are depicted in black, with the 90% isodose contour highlighted in red. The figure illustrates the dose distribution characteristics, with most combinations showing high doses near the water surface (≈ 90%). Notably, for higher energies and larger applicator diameters, the area covered by the 90% isodose is reduced.

be hinted at from the decreasing electron fluence with radial distance observed when analyzing the PSFs of large-diameter applicators.

Regarding computational efficiency, although the model optimization process requires considerable computational time, it can be substantially reduced using modern hardware featuring higher clock speeds or additional computational cores–potentially halving the required time. For clinical implementation of MC dose calculations with patient-specific anatomical information from intraoperative imaging, the PSFs generated in this study may serve as valuable inputs. However, to further accelerate these calculations, treatment planning oriented MC codes such as DPM,[41] which are specifically optimized for radiotherapy treatment planning applications, could be employed to achieve substantial speed improvements. Moreover, the current requirement of a 0.5% uncertainty in absorbed dose calculations may be unnecessarily stringent; adopting a 1% uncertainty threshold could offer an additional fourfold improvement in speed while still maintaining clinically acceptable dosimetric accuracy. With these combined optimizations, final absorbed dose calculations could be completed in just a few minutes, making MC-based dose planning more feasible for intraoperative applications.

Additionally, the PSFs for the four Liac HWL energies and various applicators have been made publicly available in a Zenodo record[37] in the IAEA PHSP format.[42] These files provide a valuable resource for further research into IORT beams and can support dose calculations in both research and clinical settings. Their availability facilitates the development and validation of MC-based treatment planning approaches, particularly as intraoperative imaging continues to evolve and gain adoption in clinical practice.

Although this study focuses on the Liac HWL accelerator, the presented modeling workflow can be applied to other intraoperative or conventional electron linacs. Users aiming to adapt this approach to different units should begin by collecting key commissioning data–OFs, PDDs, and OARs–for representative configurations. These serve as reference benchmarks for spectrum and geometry tuning. In cases where discrepancies arise, iterative refinement of the most sensitive model parameters (e.g., energy spectrum, scattering foil and exit window thickness, and linac head diameter) is recommended. Cross-checking against published data or vendor-provided simulations, when available, may also assist in diagnosing modeling inaccuracies. The workflow diagram (Figure 2) could be expanded by adding feedback loops to the optimization block, enabling re-adjustment based on site-specific measurements. This flexible strategy supports the development of accurate models even in settings where detailed manufacturer specifications are unavailable.

5 | CONCLUSIONS

Our study demonstrates that the Liac HWL mobile IOERT linac can be effectively modeled using only three geometric parameters and optimized energy spectra. The required measurements align with standard protocols for commissioning a linear accelerator for radiotherapy treatments. The approach presented in this work provides a means to fine-tune the model and extend absorbed dose calculations to nonstandard applicators that are not supported by the manufacturer's MC software. Additionally, visualizing these dose distributions can help identify potential issues with specific combinations of energy, applicator diameter, and bevel angle. While this study focuses on a specific accelerator, the methodology can serve as a reference for MC modeling of other intraoperative linacs. Beyond its use in treatment planning and commissioning, the model also supports a range of clinical and research applications. The PSFs generated at multiple energies have been made publicly available in IAEA format and offer a reliable resource for dose calculations in water and other media. Importantly, these PSFs may serve as reference datasets for benchmarking faster dose calculation algorithms. This is particularly relevant in the context of developing real-time or near-real-time planning tools for IOERT. Furthermore, the model can aid in detector development, in-vivo dosimetry validation, shielding studies, applicator design, and cross-platform benchmarking of MC implementations. Additionally, visualizing these dose distributions can help identify potential issues with specific combinations of energy, applicator diameter, and bevel angle, supporting more informed energy selection and applicator setup. This makes the model not only a research tool, but also a practical aid in addressing the real-time challenges encountered in IOERT treatment planning and beam selection.

ACKNOWLEDGMENTS

The authors acknowledge support from Spanish Government and Next Generation EU Recovery and Resilience Facility (RRF) CPP 2021-008751 NEWMBI; MCIN/AEI/10.13039/501100011033 under Grants INVENTOR (PID2022-137114OA-I00), FLASHonCHIP (PLEC2022-009256), and PROTOTWIN (TED2021-130592B-I00). The authors acknowledge support by Comunidad de Madrid, Spain under Projects ASAP-CM (S2022/BMD7434) and the European Union as part of the European Innovation Council's Pathfinder Open Programme: RETIMAGER, 101099096.

CONFLICT OF INTEREST STATEMENT

The authors declare that they have no known competing financial interests or personal relationships that could have appeared to influence the work reported in this paper.

REFERENCES

1. Palta JR, Biggs PJ, Hazle JD, et al. Intraoperative electron beam radiation therapy: Technique, dosimetry, and dose specification: report of task force 48 of the radiation therapy committee, American Association of Physicists in Medicine. *Int J Radiat Oncol Biol Phys*. 1995;33(3):725-746. doi:10.1016/0360-3016(95)00280-C
2. Calvo FA, Meirino RM, Orecchia R. Intraoperative radiation therapy. *Crit Rev Oncol/Hematol*. 2006;59(2):106-115. doi:10.1016/j.critrevonc.2005.11.004
3. Beddar AS, Biggs PJ, Chang S, et al. Intraoperative radiation therapy using mobile electron linear accelerators: report of AAPM Radiation Therapy Committee Task Group No. 72:Task Group No. 72. *Med Phys*. 2006;33(5):1476-1489. doi:10.1118/1.2194447
4. Roeder F, Morillo V, Saleh-Ebrahimi L, Calvo FA, Poortmans P, Ferrer Albiach C. Intraoperative radiation therapy (IORT) for soft tissue sarcoma – ESTRO IORT Task Force/ACROP recommendations. *Radiother Oncol*. 2020;150:293-302. doi:10.1016/j.radonc.2020.07.019
5. Fastner G, Gaisberger C, Kaiser J, et al. ESTRO IORT Task Force/ACROP recommendations for intraoperative radiation therapy with electrons (IOERT) in breast cancer. *Radiother Oncol*. 2020;149:150-157. doi:10.1016/j.radonc.2020.04.059
6. Calvo FA, Sole CV, Rutten HJ, et al. ESTRO/ACROP IORT recommendations for intraoperative radiation therapy in locally recurrent rectal cancer. *Clin Transl Radiat Oncol*. 2020;24:41-48. doi:10.1016/j.ctro.2020.06.007
7. Calvo FA, Sole CV, Rutten HJ, et al. ESTRO/ACROP IORT recommendations for intraoperative radiation therapy in primary locally advanced rectal cancer. *Clin Transl Radiat Oncol*. 2020;25:29-36. doi:10.1016/j.ctro.2020.09.001
8. Calvo FA, Krengli M, Asencio JM, et al. ESTRO IORT Task Force/ACROP recommendations for intraoperative radiation therapy in unresected pancreatic cancer. *Radiother Oncol*. 2020;148:57-64. doi:10.1016/j.radonc.2020.03.040
9. Pascau J, Santos Miranda JA, Calvo FA, et al. An Innovative Tool for Intraoperative Electron Beam Radiotherapy Simulation and Planning:description and Initial Evaluation by Radiation Oncologists. *Int J Radiat Oncol Biol Phys*. 2012;83(2):e287-e295. doi:10.1016/j.ijrobp.2011.12.063

10. Valdivieso-Casique MF, Rodríguez R, Rodríguez-Bescós S, et al. RADIANCE–A planning software for intra-operative radiation therapy. *Transl Cancer Res*. 2015;4(2):14.
11. Chetty IJ, Curran B, Cygler JE, et al. Report of the AAPM Task Group No. 105:Issues associated with clinical implementation of Monte Carlo–based photon and electron external beam treatment planning. *Med Phys*. 2007;34(12):4818-4853. doi:10.1118/1.2795842
12. Iaccarino G, Strigari L, D'Andrea M, et al. Monte Carlo Simulation of Electron Beams Generated by a 12 MeV Dedicated Mobile IORT Accelerator. *Phys Med Biol*. 2011;56(14):4579-4596. doi:10.1088/0031-9155/56/14/022
13. Robatjazi M, Tanha K, Mahdavi SR, et al. Monte carlo simulation of electron beams produced by liac intraoperative radiation therapy accelerator. *J Biomed Phys Eng*. 2018;8(1):43-52.
14. Righi S, Karaj E, Felici G, Di Martino F. Dosimetric characteristics of electron beams produced by two mobile accelerators, Novac7 and Liac, for intraoperative radiation therapy through Monte Carlo simulation. *J Appl Clin Med Phys*. 2013;14(1):6-18. doi:10.1120/jacmp.v14i1.3678
15. Ibañez García PB. *Implementation and validation of ultra-fast dosimetric tools for IORT*. PhD Thesis. Universidad Complutense de Madrid, CEI Moncloa; 2018.
16. Ayala R, García R, Ruiz G, et al. Dosimetric study of bevel factors in IOERT with mobile linacs:Towards a unified code of practice. *Physica Med*. 2024;127:104836. doi:10.1016/j.ejmp.2024.104836
17. Alhamada H, Simon S, Philippson C, et al. 3D Monte Carlo dosimetry of intraoperative electron radiation therapy (IOERT). *Physica Med*. 2019;57:207-214. doi:10.1016/j.ejmp.2018.12.037
18. Herranz E, Herraiz JL, Ibáñez P, et al. Phase space determination from measured dose data for intraoperative electron radiation therapy. *Phys Med Biol*. 2015;60(1):375-401. doi:10.1088/0031-9155/60/1/375
19. Vidal M, Ibáñez P, Guerra P, et al. Fast optimized Monte Carlo phase-space generation and dose prediction for low energy x-ray intra-operative radiation therapy. *Phys Med Biol*. 2019;64(7):075002. doi:10.1088/1361-6560/ab03e7
20. Winkler P, Odreitz-Stark S, Haas E, Thalhammer M, Partl R. Commissioning, dosimetric characterization and machine performance assessment of the LIAC HWL mobile accelerator for Intraoperative Radiotherapy. *Z Med Phys*. 2020;30(4):279-288. doi:10.1016/j.zemedi.2020.06.004
21. Di Venanzio C, Marinelli M, Tonnetti A, et al. Characterization of a microDiamond detector in high-dose-per-pulse electron beams for intra operative radiation therapy. *Physica Med*. 2015;31(8):897-902. doi:10.1016/j.ejmp.2015.06.008
22. Sempau J, Badal A, Brualla L. A PENELOPE-based system for the automated Monte Carlo simulation of clinacs and voxelized geometries–application to far-from-axis fields. *Med. Phys*. 2011;38:5887-5895. doi:10.1118/1.3643029
23. Nuclear Energy Agency. A code system for Monte Carlo simulation of electron and photon transport. *PENELOPE 2018:A Code System for Monte Carlo Simulation of Electron and Photon Transport:Workshop Proceedings, Barcelona, Spain, 28 January – 1 February 2019* . Nuclear Energy Agency; 2019.
24. Almansa J, Salvat-Pujol F, Díaz-Londoño G, Carnicer A, Lallena AM, Salvat F. PENGEOM –A general-purpose geometry package for Monte Carlo simulation of radiation transport in material systems defined by quadric surfaces. *Comput Phys Commun*. 2016;199:102-113. doi:10.1016/j.cpc.2015.09.019
25. Björk P, Kns T, Nilsson P. Influence of initial electron beam characteristics on Monte Carlo calculated absorbed dose distributions for linear accelerator electron beams. *Phys Med Biol*. 2002;47(22):4019-4041. doi:10.1088/0031-9155/47/22/308
26. Zhengming L, Jette D. On the possibility of determining an effective energy spectrum of clinical electron beams from percentage depth dose (PDD) data of broad beams. *Phys Med Biol*. 1999;44(8):N177-N182. doi:10.1088/0031-9155/44/8/401
27. Chvetsov AV, Sandison GA. Reconstruction of electron spectra using singular component decomposition. *Med Phys*. 2002;29(4):578-591. doi:10.1118/1.1461840
28. Kawrakow I, Fippel M, Friedrich K. 3D electron dose calculation using a Voxel based Monte Carlo algorithm (VMC). *Med Phys*. 1996;23(4):445-457. doi:10.1118/1.597673
29. Bush K, Zavgorodni S, Beckham W. Inference of the optimal pretarget electron beam parameters in a Monte Carlo virtual linac model through simulated annealing. *Med Phys*. 2009;36(6):2309-2319. doi:10.1118/1.3130102
30. Kirkpatrick S, Gelatt Jr CD, Vecchi MP. Optimization by simulated annealing. *Science* 1983;220(4598):671-680.
31. Tsallis C, Stariolo DA. Generalized simulated annealing. *Physica A*. 1996;233(1-2):395-406. doi:10.1016/S0378-4371(96)00271-3
32. Virtanen P, Gommers R, Oliphant TE, et al. SciPy 1.0:fundamental algorithms for scientific computing in python. *Nat Methods*. 2020;17:261-272. doi:10.1038/s41592-019-0686-2
33. Low DA, Harms WB, Mutic S, Purdy JA. A technique for the quantitative evaluation of dose distributions. *Med Phys*. 1998;25(5):656-661. doi:10.1118/1.598248
34. Biggs S, Jennings M, Swerdloff S, et al. PyMedPhys:A community effort to develop an open,Python-based standard library for Med Phys. applications. *J Open Source*. 2022;7(78):4555. doi:10.21105/joss.04555
35. Wendling M, Zijp LJ, McDermott LN, et al. A Fast algorithm for gamma evaluation in 3D. *Med Phys*. 2007;34(5):1647-1654. doi:10.1118/1.2721657
36. Micke A, Lewis DF, Yu X. Multichannel film dosimetry with nonuniformity correction: multichannel film dosimetry with nonuniformity correction. *Med Phys*. 2011;38(5):2523-2534. doi:10.1118/1.3576105
37. Ayala R. Phase space files of a Liac HWL linac. 2024. doi:10.5281/zenodo.14029135
38. Smilowitz JB, Das IJ, Feygelman V, et al. AAPM Medical Physics Practice Guideline 5.a.:commissioning and QA of Treatment Planning Dose Calculations - Megavoltage Photon and Electron Beams. *J Appl Clin Med Phys*. 2015;16(5):14-34. doi:10.1120/jacmp.v16i5.5768
39. Geurts MW, Jacqmin DJ, Jones LE, et al. AAPM medical physics practice guideline 5.b:commissioning and QA of treatment planning dose calculations–Megavoltage photon and electron beams. *J Appl Clin Med Phys*. 2022;23(9):e13641. doi:10.1002/acm2.13641
40. Oliver S, Vijande J, Tejedor-Aguilar N, et al. Monte Carlo flattening filter design to high energy intraoperative electron beam homogenization. *Radiat Phys Chem*. 2023;212:111102. doi:10.1016/j.radphyschem.2023.111102
41. Sempau J, Wilderman SJ, Bielajew AF. DPM, a fast, accurate monte carlo code optimized for photon and electron radiotherapy treatment planning dose calculations. *Phys Med Biol*. 2000;45(8):2263-2291. doi:10.1088/0031-9155/45/8/315
42. Capote R, Jeraj R, Ma C, et al. Phase-Space Database for External Beam Radiotherapy Summary Report of a Consultants' Meeting. Tech. Rep. International Atomic Energy Agency (IAEA); 2006.

How to cite this article: Ayala R, Soza Á, García MJ, García R, Udías JM, Ibáñez P. Development and validation of a Monte Carlo model of a mobile accelerator for intraoperative radiation therapy. *Med Phys*. 2025;52:e18040. https://doi.org/10.1002/mp.18040

APPENDIX: OF COMPARISON TABLES

TABLE A1 Comparison between the OFs measured with the microDiamond detector and those calculated with MC at the depth of z_{max} for the 12 MeV nominal energy. A maximum difference of 2.0% is observed for the $C_{12}B_{15}$ applicator.

Applicator diameter (cm)	Bevel angle (°)	Calculated MC OF	Measured μD OF	Diff (%)
12	0	0.916	0.901	1.7
	15	0.920	0.902	2.0
	30	0.942	0.925	1.8
	45	0.992	0.975	1.7
10	0	1.000	1.000	0.0
	15	1.011	1.003	−0.1
	30	1.034	1.023	0.6
	45	1.082	1.084	−1.0
9	0	1.066	1.064	0.2
	15	1.074	1.067	0.6
	30	1.100	1.102	−0.2
	45	1.149	1.155	−0.5
8	0	1.151	1.141	0.9
	15	1.157	1.142	1.3
	30	1.186	1.178	0.7
	45	1.245	1.236	0.7
7	0	1.252	1.238	1.2
	15	1.265	1.251	1.1
	30	1.293	1.286	0.5
	45	1.353	1.354	−0.1
6	0	1.351	1.328	1.7
	15	1.363	1.341	1.7
	30	1.395	1.389	0.5
	45	1.461	1.451	0.7
5	0	1.438	1.429	0.7
	15	1.452	1.439	0.9
	30	1.485	1.474	0.7
	45	1.548	1.534	0.9
4	0	1.505	1.495	0.7
	15	1.516	1.503	0.9
	30	1.544	1.542	0.1
	45	1.598	1.605	−0.5
3	0	1.502	1.484	1.2
	15	1.510	1.487	1.6
	30	1.533	1.509	1.6
	45	1.573	1.568	0.3

(Continues)

TABLE A1 (Continued)

Abbreviation: OFs, output factor.

TABLE A2 Comparison between the OFs measured with the microDiamond detector and those calculated with MC at the depth of z_{max} for the 10 MeV nominal energy. A maximum difference of -2.5% is observed for the C_4B_{45} applicator.

Applicator diameter (cm)	Bevel angle (°)	Calculated MC OF	Measured μD OF	Diff (%)
12	0	0.896	0.888	0.9
	15	0.903	0.883	2.3
	30	0.928	0.910	2.1
	45	0.977	0.963	1.5
10	0	1.000	1.000	0.0
	15	1.004	1.003	0.1
	30	1.029	1.025	0.4
	45	1.079	1.089	−1.0
9	0	1.068	1.062	0.6
	15	1.077	1.062	1.3
	30	1.105	1.105	0.0
	45	1.154	1.159	−0.4
8	0	1.158	1.153	0.4
	15	1.166	1.168	−0.2
	30	1.197	1.215	−1.5
	45	1.249	1.245	0.3
7	0	1.260	1.249	0.9
	15	1.275	1.270	0.4
	30	1.311	1.310	0.1
	45	1.372	1.373	−0.1
6	0	1.353	1.335	1.4
	15	1.365	1.370	−0.4
	30	1.403	1.424	−1.4
	45	1.471	1.498	−1.8
5	0	1.430	1.419	0.7
	15	1.442	1.438	0.3
	30	1.478	1.466	0.8
	45	1.551	1.535	1.1
4	0	1.474	1.463	0.8
	15	1.483	1.507	−1.6
	30	1.508	1.541	−2.2
	45	1.573	1.613	−2.5
3	0	1.423	1.412	0.8
	15	1.427	1.418	0.6

(Continues)

TABLE A2 (Continued)

Applicator diameter (cm)	Bevel angle (°)	Calculated MC OF	Measured μD OF	Diff (%)
	30	1.446	1.435	0.8
	45	1.489	1.497	−0.5

Abbreviation: OFs, output factor.

TABLE A3 Comparison between the OFs measured with the microDiamond detector and those calculated with MC at the depth of z_{max} for the 8 MeV nominal energy. A maximum difference of 2.2% is observed for the $C_{12}B_{15}$ applicator.

Applicator diameter (cm)	Bevel angle (°)	Calculated MC OF	Measured μD OF	Diff (%)
12	0	0.889	0.883	0.7
	15	0.897	0.878	2.2
	30	0.921	0.913	0.8
	45	0.964	0.962	0.2
10	0	1.000	1.000	0.0
	15	1.007	1.003	0.3
	30	1.033	1.030	0.3
	45	1.073	1.094	−1.9
9	0	1.078	1.067	1.0
	15	1.085	1.067	1.7
	30	1.109	1.109	0.0
	45	1.155	1.167	−1.0
8	0	1.163	1.165	−0.1
	15	1.173	1.182	−0.7
	30	1.205	1.220	−1.3
	45	1.254	1.270	−1.3
7	0	1.271	1.257	1.1
	15	1.282	1.283	0.0
	30	1.316	1.318	−0.1
	45	1.372	1.381	−0.6
6	0	1.357	1.334	1.7
	15	1.371	1.366	0.4
	30	1.406	1.419	−0.9
	45	1.468	1.493	−1.7
5	0	1.417	1.394	1.6
	15	1.430	1.410	1.4
	30	1.461	1.441	1.4
	45	1.523	1.513	0.6
4	0	1.425	1.421	0.2
	15	1.433	1.443	−0.7
	30	1.462	1.483	−1.4
	45	1.529	1.552	−1.5
3	0	1.329	1.316	1.0
	15	1.329	1.317	0.9
	30	1.347	1.339	0.5
	45	1.395	1.407	−0.9

Abbreviation: OFs, output factor.

TABLE A4 Comparison between the OFs measured with the microDiamond detector and those calculated with MC at the depth of z_{max} for the 6 MeV nominal energy. A maximum difference of −2.5% is observed for the C_4B_{30} applicator.

Applicator diameter (cm)	Bevel angle (°)	Calculated MC OF	Measured μD OF	Diff (%)
12	0	0.879	0.873	0.6
	15	0.886	0.870	1.8
	30	0.908	0.903	0.5
	45	0.953	0.953	0.0
10	0	1.000	1.000	0.0
	15	1.011	1.005	0.6
	30	1.034	1.029	0.5
	45	1.082	1.086	−0.4
9	0	1.074	1.065	0.8
	15	1.082	1.066	1.5
	30	1.110	1.100	0.9
	45	1.156	1.160	−0.4
8	0	1.162	1.160	−1.0
	15	1.178	1.166	−1.3
	30	1.208	1.203	0.3
	45	1.257	1.270	0.7
7	0	1.260	1.249	−0.7
	15	1.272	1.275	−0.6
	30	1.307	1.305	−0.1
	45	1.362	1.371	−0.1
6	0	1.331	1.305	−0.8
	15	1.343	1.329	−1.7
	30	1.376	1.376	−1.8
	45	1.439	1.451	0.7
5	0	1.370	1.357	−0.6
	15	1.383	1.380	0.6
	30	1.419	1.418	1.1
	45	1.483	1.492	0.9
4	0	1.353	1.347	−1.4
	15	1.362	1.374	−1.5
	30	1.396	1.407	−2.5
	45	1.447	1.467	−0.5
3	0	1.215	1.202	1.1
	15	1.225	1.204	−0.9
	30	1.246	1.228	−0.5
	45	1.301	1.287	−2.2

Abbreviation: OFs, output factor.